Universiteit Utrecht

Faculty of Science

Influence of tidal currents on transport and accumulation of floating microplastics in the ocean

Bachelor thesis

M.F. Sterl

Physics and Astronomy

Supervisors:

Dr. E. van Sebille
Institute for Marine and Atmospheric Research Utrecht

Dr. P.B. Delandmeter
Institute for Marine and Atmospheric Research Utrecht

January 2019

Abstract

Floating plastic debris is becoming an increasing source of pollution of the world's oceans that can seriously harm marine life. To understand the severity of the problem and find suitable solutions, knowledge of the sources, pathways and fate of plastic in oceans is required. However, observational data about floating plastic in marine environments are hard to obtain, especially for microplastics (smaller than 5 mm in size). Instead, numerical simulations using models of ocean currents are a key tool to gain insight into the transport and distribution of microplastics in oceans. Most models used for such simulations do not account for flow caused by global tides. In this project, we investigate the influence of tidal currents on the transport and accumulation of floating microplastics. We do this by numerically simulating the advection of particles released all over the world's oceans for 13 years. We use data from the GlobCurrent reanalysis project to model geostrophic and Ekman currents, and from the FES global tidal model to model currents caused by the four main tidal constituents (M_2, S_2, K_1 and O_1). We analyse the differences between the outcomes of runs with and without these tidal currents included. In each of the runs, we see that microplastic accumulates in so-called garbage patches in the subtropical gyres, which is in agreement with observations. The formation of these garbage patches remains unaffected by the tidal currents. However, there are a number of coastal areas where, on different timescales, clear differences can be seen in particle density, distance travelled by particles, and the separation between particles released at the same location between the runs with and without tides. We show that the differences observed in these regions are caused by the presence of tidal currents. These results suggest that tidal currents have little impact on the transport and accumulation of floating microplastic on a global scale, but might be relevant to include in simulations and research aimed at the behaviour of microplastics in coastal environments.

Cover: C.E. Sterl (2019), *Plastic Tide* [acrylic colour and sand on canvas, 18 × 13 cm].

Contents

1 Introduction

Pollution of marine environments caused by floating plastic debris is a global problem of increasing concern. Plastic litter can enter the oceans from land-based sources or entry points (including beaches, rivers, and agricultural runoff) or sea-based sources (such as ships, platforms and fishing piers) [1], and are now one of the most common and persistent pollutants in the global ocean. Plastic waste floating at the ocean surface can significantly harm the near-surface ocean environment, especially marine life. There are 267 species of marine organisms known to be affected by plastic debris, through ingestion of plastics or entanglement in fishing nets or lines [2]. Estimates are that 275 million metric tons of plastic waste were produced in 2010, of which 4.8 to 12.7 million metric tons entered the ocean; the prediction is that without improvements in waste management, the quantity of plastic litter that can enter the ocean from land will have increased by an order of magnitude in 2025 [3]. Other estimates are that there is a minimum of 5.25 trillion plastic particles weighing 268,940 tons in the oceans in 2014 [4]. Marine plastic debris is divided into two categories: macroplastics, which are larger than 5 mm in diameter, and microplastics, smaller than 5 mm [2, 5]. Some plastics are already manufactured as microscopic particles, but microplastics can also originate from macroplastics degraded by UV radiation or chemical processes or fragmented by wave action [1, 5, 6]. Many studies have shown that convergence of surface Ekman flow causes plastic debris (macro- as well as microplastics) to accumulate in so-called *garbage patches*, found in each of the five subtropical ocean gyres, where it can remain trapped for decades to millennia [5, 6, 7, 8, 9].

Understanding the severity of the harm marine plastic litter can cause, and finding solutions to the growing problem of plastic waste accumulating in the oceans, requires knowledge of the sources, pathways and fate of plastics. However, plastic sampling and monitoring in marine environments is challenging, and samples can be highly variable because of the ever changing ocean currents [1]. In most of the world's oceans, data on plastic debris are very scarce [5]. Sampling microplastics is especially hard as they are not easily observable due to their small size. It is therefore very challenging to study microplastic abundance, distributions and pathways purely from observational data. Instead, simulations using numerical models of ocean currents can help us improve our understanding of microplastics in marine environments [1]. Many of these simulations use models for the geostrophic currents and Ekman currents. However, a group of currents that are often not included, and have not been studied before in the context of microplastic transport, are tidal currents. These currents, caused by tidal forces, are smaller in magnitude than geostrophic and Ekman currents, and could therefore be expected to have a small influence on the transport of microplastic. Nonetheless, tidal currents are in general strongest in coastal areas, which are very interesting areas in the light of plastic transport and accumulation [10]. One reason for this is that approximately half of the world's population lives near the coast, so microplastics have a high probability of entering the ocean in coastal environments [11]. Furthermore, many of the plastics released into the ocean stay near the coastline for a long time [7], and high relative concentrations of microplastics have been observed in near-shore areas [12, 13]. Studying the influence of tidal currents on the transport of microplastics can be useful to help us understand the pathways and distribution of microplastics in oceans. Moreover, it can help us determine the relevance of including tidal currents in simulations used to investigate the transport of microplastic waste.

In this project, we investigate the impact of tidal currents on the pathways and fate of microplastics in the global ocean, on short as well as long timescales. We do this by simulating the advection of microplastic particles by ocean surface currents and comparing the outcomes with and without tidal currents included. The currents used are the geostrophic and Ekman currents and the four main constituents of the tidal currents; the necessary data for the velocities of these currents are obtained from existing datasets. In Section 2, we discuss the theory of tidal forces and currents. Then, in Section 3, we give an overview of the datasets and methods used. In Section 4, the results are presented and discussed. Finally, in Section 5, we give conclusions, points of discussion and recommendations for future research.

2 Theoretical background

2.1 Tidal forces

Global ocean tides are caused by interactions between the Earth and other celestial bodies, the most important ones being the Moon and the Sun. Consider the system consisting only of the Earth and one other celestial body, which we will call B. Both bodies rotate about their common centre of mass. Since all points on the Earth rotate about this centre of mass, they all experience the same centrifugal force caused by the other body's gravity.[1] This centrifugal force has the same magnitude and direction at all these points. It exactly balances the force of gravitational attraction exerted by B on the Earth's centre, so the system is in equilibrium. The centrifugal force is therefore given by

$$\vec{F}_{\mathrm{cf}} = -\vec{F}_{\mathrm{g}}^{B\to\text{Earth centre}} = -GMm\frac{\hat{R}}{R^2}, \tag{1}$$

where G is the gravitational constant, M is the mass of B, m is the mass of the Earth, R is the distance between the Earth's centre and B's centre, and $\hat{R}$ is the unit vector in this direction. The $-$sign indicates that the force is directed away from B. Apart from this force, every point on the Earth's surface also experiences the gravitational force exerted by B, which is given by

$$\vec{F}_{\mathrm{g}}^{B\to\text{Earth}} = GMm\frac{\hat{r}}{r^2}, \tag{2}$$

where r is now the distance between a specific point on the Earth's surface and the centre of B, and $\hat{r}$ is the unit vector in that direction. Note that the magnitude and direction of this force will vary over the Earth's surface. The resultant of the centrifugal force and the gravitational force caused by B is called the *tidal force* [14, 15]:

$$\vec{F}_{\mathrm{tidal}} = GMm\left(\frac{\hat{r}}{r^2} - \frac{\hat{R}}{R^2}\right). \tag{3}$$

The effect of the tidal force is visualised in Figure 1. In this figure, point C is the centre of the Earth; here the centrifugal force and the gravitational force caused by B cancel exactly. Points P and Q lie on the line joining the centres of B and the Earth, so $\hat{R} = \hat{r}$. In point P, which is closest to B, the tidal force is directed towards B; in point Q it is directed away from it. In points S and T, which lie on a line that makes a right angle with $\hat{R}$, the component of the gravitational force tangent to the Earth's surface cancels the centrifugal force, and the resultant force points inward to the Earth's centre.

In the simplified case where we assume the Earth's surface to be covered with water, an equilibrium state would be reached, in which the Earth's surface water would be deformed with two 'tidal bulges' at points P and Q. This state is called the *equilibrium tide* [15]. As the Earth rotates around its own axis, these tidal bulges move over the Earth's surface. This is a periodic process; since celestial motion is on the whole periodic, so are tidal phenomena. So as a result of tidal forces, we observe periodic raising and lowering of the ocean's water levels. Moreover, this vertical rise and fall of the tides causes horizontal motion of the ocean's surface, which we call *tidal currents* [15, 16]. The tidal velocity currents can be related to the tidal height of the ocean's surface using shallow-water theory [17].

We can approximate the magnitude of the tidal force at high tide by making a Taylor expansion for point P. Here $\hat{r} = \hat{R}$, and $r = R - a$, where a is the Earth radius. Making use of the fact that a is much smaller than the distance R from the Earth's centre to the Moon, Sun or any planet, we get

$$F_{\mathrm{tidal},P} = GMm\left(\frac{1}{(R-a)^2} - \frac{1}{R^2}\right) = \frac{GMm}{R^2}\left(1 - \left(1 - \frac{a}{R}\right)^{-2}\right) \approx \frac{2GMma}{R^3} + \mathcal{O}\left(\frac{a^2}{R^2}\right). \tag{4}$$

[1]This rotational motion is not to be confused with the Earth's rotation about its own axis.

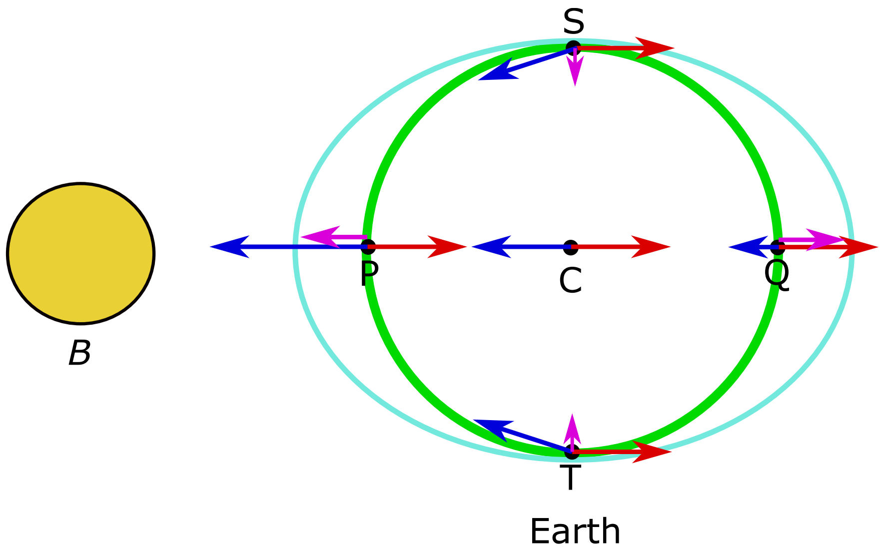

Figure 1: Visualisation of the effect of the tidal force. Red arrows indicate the centrifugal force due to rotation about the common centre of mass of the Earth and body B; it has the same direction and magnitude everywhere on Earth. Blue arrows indicate the gravitational force caused by B, which is stronger in points closer to B. Purple arrows show the resultant of the centrifugal and gravitational force: this is the tidal force. The light blue line shows how the water on the Earth's surface is deformed by the tidal force.

So the intensity of the tidal force is proportional to the mass M of B and inversely proportional to the cube of the distance R between the Earth and B. This explains why the Moon, which has less mass than the Sun and the planets but is much closer to the Earth, causes the strongest tidal force. The second-strongest tidal force is caused by the Sun, and has a magnitude of approximately half of the lunar tidal force. Tidal forces caused by the other planets are very small compared to the lunar and solar tidal forces. Venus is the planet with the strongest tidal force because it comes closest to the Earth. However, even if Venus is at its minimum distance to the Earth, its tidal force is five orders of magnitude smaller than that of the Sun and Moon together. So, for all intents and purposes, the tides observed on Earth are the superposition of the tides caused by the Moon and those caused by the Sun.

As mentioned before, the tidal bulges move over the Earth's surface as the Earth rotates around its own axis. If the Earth were a perfect sphere with only water at its surface, all points on the surface would experience two high and low tides a day. However, the real situation is more complex, and actual tides do not behave as equilibrium tides. The Earth's large continents block the passage of the tidal bulges, and the tides are therefore confined in their movements [14, 15]. Another complication is introduced by the inclination of the Earth's axis and the Moon's orbit: the tidal bulges are not exactly parallel to the Equator, but at some angle to it. As a result, in the course of one day a point on the Earth's surface will experience *one* absolute maximum of the tidal force instead of two [16]. Moreover, the magnitude of the tides can be influenced by many different factors, such as astronomical variations, the shape of shorelines, bays and estuaries, and local wind and weather patterns [15, 18].

2.2 Harmonic analysis of the tides

Variations in the relative positions and orientations of the Earth, Moon and Sun according to different interacting cycles cause temporal variations in the tides. Examples of such periodic variations are the regular changes in the declinations of the Sun and the Moon and the elliptical motion of the Moon around the Earth and the Earth around the Sun. These astronomical cycles produce a great number of *tidal constituents* contributing to the tides, each of which has a period corresponding with the period of one of these cycles [15]. The global tide can be decomposed into these tidal constituents by using *harmonic analysis*. Harmonic analysis is based upon the assumption that the tidal height of the water surface can be decomposed into a number of harmonic components. As the tidal currents are caused by the same periodic forces that cause the periodic rise and fall of the tide, they can also be represented by harmonic expressions. The equations for the horizontal tidal velocity currents U and V at any time t and at any location $\vec{x}$ are given by the following expressions [16, 19]:

$$U(\vec{x}, t) = \sum_i f_i(t) A_i^U(\vec{x}) \cos\left[\omega_i(t - t_0) + u_i(t) + V_i(t_0) - \varphi_i^U(\vec{x})\right], \tag{5}$$

$$V(\vec{x}, t) = \sum_i f_i(t) A_i^V(\vec{x}) \cos\left[\omega_i(t - t_0) + u_i(t) + V_i(t_0) - \varphi_i^V(\vec{x})\right]. \tag{6}$$

Here, U and V denote the zonal and meridional velocity caused by the tidal forces, respectively. The location on Earth (latitude and longitude) is denoted by the vector $\vec{x}$. The variable t represents the time, measured with respect to some initial time t_0. The index i is over the different tidal constituents, all of which have their own angular frequency ω_i, which relates to their period T_i as $\omega_i = 2\pi/T_i$. The coefficients A_i^U and A_i^V are the amplitudes (maximum velocities) of constituent i; φ_i^U and φ_i^V are the initial phases or phase shifts (fraction of the tidal constituent's cycle that has been completed) of constituent i at time t_0. These amplitudes and phase shifts depend on longitude and latitude, and can be determined from observational data.

Then, there are a number of time-dependent correction factors. The *astronomical argument correction* $V_i(t_0)$ re-expresses the phase shifts with respect to an absolute time origin (t_0) [20]. The variables $f_i(t)$ and $u_i(t)$ are the *nodal modulation amplitude* and *phase corrections*, respectively, and account for the slow time evolution of the amplitude and phase of a constituent. When applying harmonic analysis to determine the different tidal constituents, hundreds of tidal constituents can be taken into account. As there are so many, for practical purposes constituents are grouped together into *constituent clusters* consisting of constituents with very nearly equal frequencies. In theory, an analysis of 19 years[2] of observations would be needed to separate all the constituent of such a cluster. In practice, however, due to the very small amplitudes of some constituents, the presence of noise in measurements, and geological and oceonagraphic changes to the tides which become significant over such a long period, it is impossible to analyse every constituent separately [16]. Therefore, it is assumed that as a first approximation, each cluster can be replaced by one harmonic component with the frequency of the constituent with the largest amplitude. However, because the measured amplitude and phase shift of this main constituent actually represent the cumulative effect of all constituents in the cluster, an adjustment is made so that only the contribution due to the main constituent is found. This adjustment is called the *nodal modulation* for the amplitude and phase [20, 21].

[2] All nodal modulation amplitudes have a period of at most 19 years [16].

2.3 Calculation of the main tidal currents

There exist a great number of tidal constituents; Doodson [22] distinguished as many as 388 different constituents [23]. Two of the most important tidal constituents in the sense of largest amplitude are the M_2 tide, or *semi-diurnal lunar tide*, and the S_2 tide, or *semi-diurnal solar tide*. The M_2 tide is caused by forcing due to the Moon and its angular frequency is $\omega_{M_2} = 28.9841042°$/hour, which corresponds to a period of half a lunar day (12 h 25 m). Likewise, the S_2 tide is the result of forcing by the Sun; it has angular frequency $\omega_{S_2} = 30.0000000°$/hour, and period half a solar day (12 h) [19]. As the M_2 and S_2 tides move in and out of phase, they cause the *spring-neap cycle*, a 14.8 day cycle during which the tidal forces caused by the Sun and the Moon either reinforce each other (*spring tides* or *spring currents*) or partially cancel each other (*neap tides* or *neap currents*) [16]. Two other important constituents are the K_1 tide, or *diurnal luni-solar tide*, and the O_1 tide, or *diurnal lunar tide*. These tides are related to the inclinations of the Earth's axis and the Moon's orbit (see also Section 2.1). Their frequencies are $\omega_{K_1} = 15.0410686°$/hour and $\omega_{O_1} = 13.9430356°$/hour, respectively [19]. Since the Moon causes the strongest tidal force (see Section 2.1), the M_2 constituent has the largest amplitude of all tidal constituents. The K_1 tide has the second-largest amplitude, which is 58.4% of the M_2 amplitude. The S_2 and O_1 tide follow in third and fourth place, respectively, with 46.6% and 41.5% of the M_2 amplitude.

Because these are the main tidal constituents, as a first approximation only the M_2, S_2, K_1 and O_1 constituents are taken into account for the computation of tidal velocity fields. Henceforth, we will refer to these four constituents as the *main tidal constituents*, and to the currents they cause as the *main tidal currents*. Data for the amplitudes and phase shifts of the main tidal currents are obtained from the TPXO7.2 dataset [27] and the FES2014 dataset [28] (see Section 3.2 for more information). The astronomical argument correction and nodal modulation amplitude and phase corrections can be calculated from a number of astronomical variables [21]:

$$\begin{aligned}
T(t)&, \text{ solar angle relative to Greenwich;}\\
h(t)&, \text{ longitude of the Sun;}\\
s(t)&, \text{ longitude of the Moon;}\\
N(t)&, \text{ longitude of the Moon's ascending node.}
\end{aligned}$$

For our calculations, we take the origin of time t_0 to be January 1, 1900, 00:00:00 UTC. For each time t, let $\tau = t - t_0$ be the time that has passed since t_0, expressed in number of Julian centuries (36,525 days). Then the astronomical variables defined above can be calculated as

$$T(t) = 180.0° + 36525 \cdot 360.0°\tau, \tag{7}$$
$$h(t) = 280.1895015° + 36000.76892°\tau, \tag{8}$$
$$s(t) = 277.0256206° + 481267.892°\tau, \tag{9}$$
$$N(t) = 259.1560563° - 1934.1423972°\tau. \tag{10}$$

These constants are taken from the code accompanying the FES2014 dataset [28]. They can also be found in Doodson (1921) [22], where some of the values are slightly different from those in the FES2014 code (differences occurring in the third decimal); since the FES2014 code is more recent, it is assumed that the values used there are the results of more precise measurements, so these values are used for the calculations.

For the calculation of the nodal modulations, we also need four more variables I, ξ, ν and ν', which can be calculated from $N(t)$ using the following relations [19]:

$$\cos I = 0.91370 - 0.03569 \cos N, \tag{11}$$

$$\tan\left(\frac{N-\xi+\nu}{2}\right) = 1.01883 \tan\left(N/2\right), \tag{12}$$

$$\tan\left(\frac{N-\xi-\nu}{2}\right) = 0.64412 \tan\left(N/2\right), \tag{13}$$

$$\tan \nu' = \frac{\sin(2I)\sin(\nu)}{\sin(2I)\cos(\nu) + 0.3347}. \tag{14}$$

From these numbers, we can calculate the values of $V(t)$, $u(t)$ and $f(t)$ for each of the main tidal constituents. The formulas for these calculations are listed in Table 1.

	V	u	f
$\mathbf{M}_2$	$2T - 2s + 2h$	$2\xi - 2\nu$	$1.0924\cos^4(I/2)$
$\mathbf{S}_2$	$2T$	0	1
$\mathbf{K}_1$	$T + h - 90°$	$-\nu'$	$\sqrt{0.8965\sin^2(I) + 0.6001\sin(2I)\cos(\nu) + 0.1006}$
$\mathbf{O}_1$	$T - 2s + h + 90°$	$2\xi - \nu$	$2.6316\sin(I)\cos^2(I/2)$

Table 1: The expressions for the astronomical argument correction $V(t)$, the nodal modulation phase correction $u(t)$ and the nodal modulation amplitude correction $f(t)$ for the M_2, S_2, K_1 and O_1 tidal constituents.

All these formulas are taken from [19]. For further background and discussion on these formulas, we refer to [16] and [19]. The total eastward and northward currents due to the four main tidal constituents can now be calculated for every location and every time using Equations (5) and (6), where $i = \mathrm{M}_2, \mathrm{S}_2, \mathrm{K}_1, \mathrm{O}_1$, using observational data for A_i^U, A_i^V, φ_i^U and φ_i^V and with V_i, u_i and f_i calculated as in Table 1.

3 Data and methods

3.1 Dataset for geostrophic and Ekman currents

We use the GlobCurrent v3 dataset for ocean surface currents for the period of 2002-2014. This dataset contains values of the eastward and northward velocity components at the ocean surface on a global grid with spatial resolution 1/4°, and with a temporal resolution of 1 day. All these data are from the GlobCurrent project, which combines satellite measurements with in-situ measurements to obtain estimates of ocean surface currents [24]. First, an initial estimate of geostrophic velocities is derived from altimeter maps. These velocities are then subtracted from the surface velocities of ARGO floats to get an estimate of the Ekman velocity at the surface. The Ekman velocity at depth z, $\vec{u}_{\mathrm{Ek}}(z)$, is modelled using a two-parameter formulation [25]:

$$\vec{u}_{\mathrm{Ek}}(z) = \beta(z)\vec{\tau}e^{i\theta(z)} \tag{15}$$

The parameters $\beta(z)$ and $\theta(z)$ at the surface $z = 0$ are estimated by fitting the model to the initial estimates of the surface Ekman velocities, using wind stress data from ERA-Interim [26]. Using the velocities of 841,786 ARGO floats, the surface Ekman currents are found to be at an angle of $\theta(z = 0) = 30.75°$ to the wind stress direction (to the right on the Northern Hemisphere, to left on the Southern Hemisphere), with an amplitude factor $\beta(z = 0) = 0.61\ \mathrm{m^2s/kg}$. The geostrophic velocities are now calculated by subtracting the obtained Ekman surface velocities from the velocities of surface drifters from the Surface Velocity Program (SVP). Finally, the total surface currents are the sum of the geostrophic velocities and the surface Ekman velocities [25]. The magnitude of the total surface velocities from the GlobCurrent v3 dataset averaged over the period 2002-2014 is shown in Figure 2.

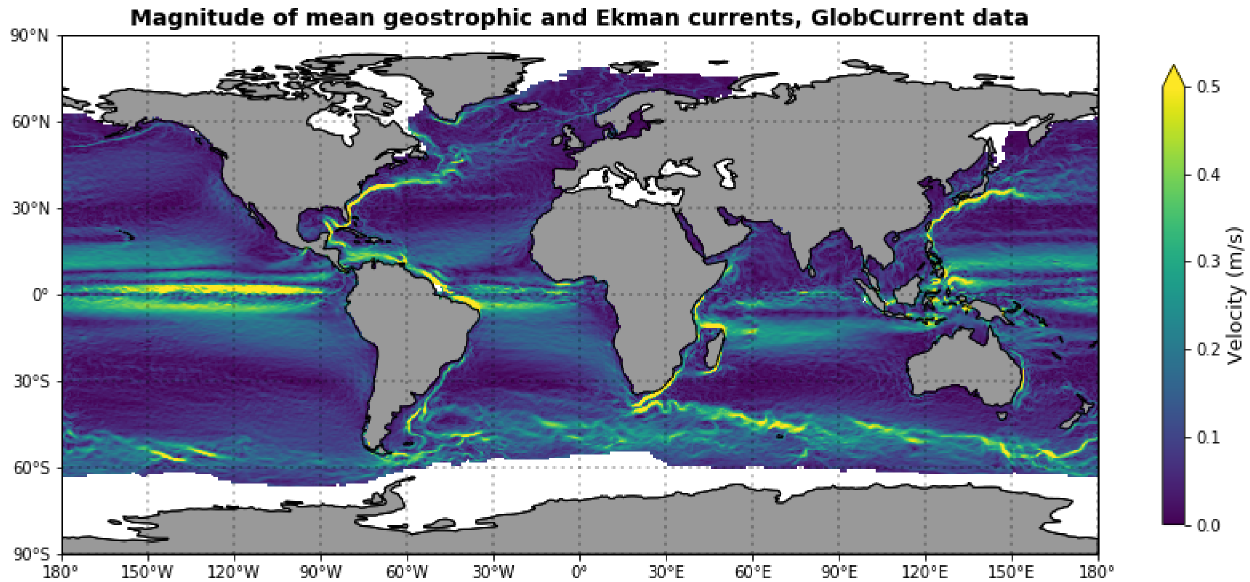

Figure 2: The magnitude of the time-averaged geostrophic and Ekman currents from the GlobCurrent v3 dataset. Time averages are computed for the years 2002-2014.

3.2 Dataset for tidal currents

For the tidal currents, we considered two different datasets: the TPXO7.2 dataset [27] and the FES2014 dataset [28]. Both datasets are based on fitting to theoretical models (see Section 2) and data assimilation from satellite altimetry and tide gauges (which measure the change in sea level relative to some reference level), and they contain the amplitudes and phase shifts of the eastward and northward velocity component of a number of tidal constituents (13 constituents in case of TPXO7.2 and 34 in case of FES2014). The spatial resolution of the grid is 1/4° for TPXO7.2 and 1/16° for FES2014. For this project, only the M_2, S_2, K_1 and O_1 constituents are taken into account. Comparisons show that the amplitude and phase shift data for these constituents are almost equal for both datasets, and only small differences can be seen[3] (see Appendix B.2). Since the FES2014 dataset is defined on a grid with a higher spatial resolution than TPXO7.2, we will use FES2014 in this project. (Nevertheless, we do use a time series generated from TPXO7.2 with existing software to test our own FES2014-processing code; see Section 3.4.1.) Note that the amplitudes and phase shifts from these data depend only on latitude and longitude (see Equations (5) and (6)). The full space- and time-dependent main tidal currents are calculated as discussed in Section 2.3.

The eastward and northward velocity amplitudes of the main tidal constituents from the FES2014 dataset are shown in Figure 3 and 4. An interesting observation from these figures is that the amplitudes are largest in coastal areas and that they are very small in the open ocean. In some coastal areas, the M_2 amplitudes are of order 0.1 m/s. Comparing with Figure 2, we see that it is only in these coastal areas that the tidal currents have the same order of magnitude as the geostrophic and Ekman currents; elsewhere, they are two orders of magnitude smaller. Furthermore, the amplitudes of the S_2, K_1 and O_1 tide are small compared to those of the M_2 tide.

[3] One difference is that the FES2014 dataset contains data for the Black Sea, whereas the TPXO7.2 dataset does not. However, as the Black Sea is not part of the global ocean, we will not release particles there in our simulations, so for this project it doesn't make a difference.

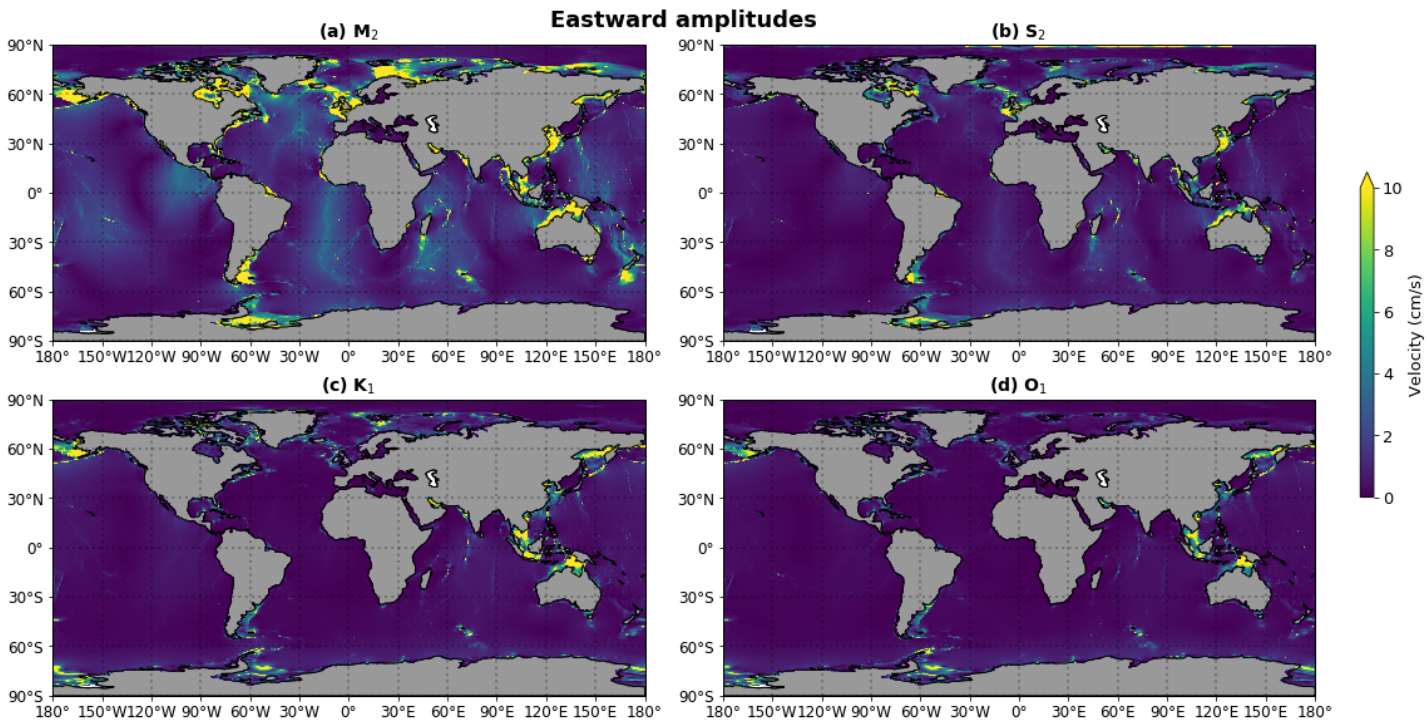

Figure 3: The eastward velocity amplitudes A^U of the M_2, S_2, K_1 and O_1 tidal currents from the FES2014 dataset.

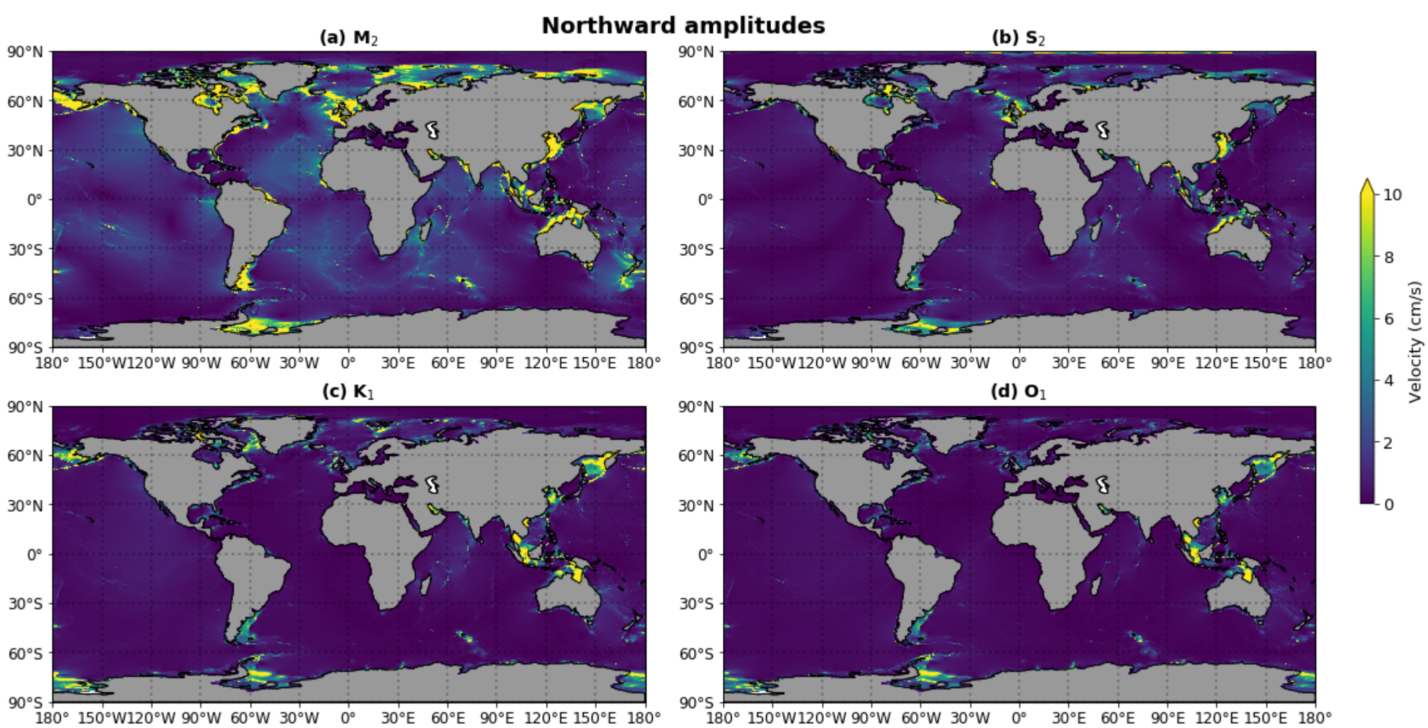

Figure 4: The northward velocity amplitudes A^V of the M_2, S_2, K_1 and O_1 tidal currents from the FES2014 dataset.

3.3 Particle tracking simulations

For our numerical simulations, we use Parcels (Probably A Really Efficient Lagrangian Simulator) [29] to model microplastics as virtual particles which are advected using ocean flow field data. Parcels computes Lagrangian particle trajectories using the formula

$$\vec{x}(t+\Delta t) = \vec{x}(t) + \int_t^{t+\Delta t} \vec{v}\left(\vec{x}(\tau), \tau\right) \, \mathrm{d}\tau, \tag{16}$$

where $\vec{x}(t)$ is the particle location at time t and $\vec{v}(\vec{x}(t), t)$ is the velocity field at location $\vec{x}$ and time t, which is obtained by linear interpolation of the velocity field data. In this project, $\vec{v}$ is the sum of the geostrophic and Ekman velocities and the tidal current velocities. An important note is that all the currents used here are two-dimensional; the model does not account for vertical motion such as sinking, and thus all the particles in the simulation will stay on the ocean surface. For the geostrophic and Ekman velocities, we use flow field data from the GlobCurrent v3 dataset (see Section 3.1). To model particle advection by tidal currents, we write a function that for every time step computes the zonal and meridional velocities caused by the main tidal constituents at that time at the particle location (as described in Section 2.3), using the data from FES2014 for the amplitudes and phase shifts. The code used for this can be found in Appendix A.

To calculate the particle trajectories as in Equation (16), we use the classical *Runge-Kutta method* (RK4). This method uses the weighted average of values of $\vec{v}$ at intermittent points between t and $t + \Delta t$. The calculation is as follows [30]:

$$\begin{aligned}
\vec{X}_1 &= \vec{x}(t), \\
\vec{X}_2 &= \vec{x}(t) + \frac{\Delta t}{2} \cdot \vec{v}\left(\vec{X}_1, t\right), \\
\vec{X}_3 &= \vec{x}(t) + \frac{\Delta t}{2} \cdot \vec{v}\left(\vec{X}_2, t + \frac{\Delta t}{2}\right), \\
\vec{X}_4 &= \vec{x}(t) + \Delta t \cdot \vec{v}\left(\vec{X}_3, t + \frac{\Delta t}{2}\right), \\
\vec{x}(t+\Delta t) &= \vec{x}(t) + \frac{\Delta t}{6} \cdot \left[\vec{v}\left(\vec{X}_1, t\right) + 2 \cdot \vec{v}\left(\vec{X}_2, t + \frac{\Delta t}{2}\right) + 2 \cdot \vec{v}\left(\vec{X}_3, t + \frac{\Delta t}{2}\right) + \vec{v}\left(\vec{X}_4, t + \Delta t\right)\right].
\end{aligned}$$

RK4 is a fourth-order method; in other words, its accuracy is of order $\mathcal{O}\left((\Delta t)^4\right)$.

In our simulations, we release an initial homogeneous microplastic distribution, with particles placed in oceans at 1° intervals for latitudes between 75°S and 75°N, and longitudes between 179.75°W and 179.75°E (34,370 particles in total). To investigate the influence of tides on the transport and trajectories of microplastic, we do a number of different runs: one where the particles are advected only by the geostrophic and Ekman currents, one where they are advected only by the main tidal currents, and one with all these currents combined. For simplicity, these runs will henceforth be referred to as the GC (GlobCurrent) run, the FES run, and the GC+FES run, respectively. Then, an extra run is done with the same conditions as the GC+FES run, but now the advection by tidal currents is included only for the first 30 days; we will call this the GC+FES30 run. Effectively, we change the initial positions of the particles in this run. What we then see is how small changes in initial position impact the final distribution. The difference patterns between this run and the GC run should look like random noise. If the differences between the GC+FES run and the GC run are larger than the differences between the GC+FES30 run and the GC run, they have a clear cause that lies in the presence of tidal currents. In each case, we track the particles from our initial distribution for 13 years (January 1, 2002 − January 1, 2015), with time step $\Delta t = 30$ minutes. For every two days, the position of each particle (longitude and latitude) and the distance it has travelled at that time since the beginning of the run are saved.

Finally, we use an artificial anti-beaching boundary current that pushes particles away from the coast and thus prevents them from beaching. (In our runs, a particle beaches if it reaches a land point and gets stuck because there are no flow field data there.) This anti-beaching current is normal to the coastline and has a magnitude of 1 ms^{-1} at the coast, and it is zero everywhere else. The main reason to implement the anti-beaching current is that the investigation of particle beaching is beyond the scope of this project; a physical model for beaching is not implemented in our runs. Moreover, comparisons of runs with and without the anti-beaching current show that without it, approximately 40% of the particles beach, whereas with the anti-beaching current only 1% do.[4] Thus, the anti-beaching current allows for more robust statistics in studying the pathways and distribution of microplastic with or without influence from the tides.

3.4 Test runs

3.4.1 Time series test

To test if our modelling of tidal currents is correct, we generate a time series for the tidal currents of one month and compare it to a reference time series. The reference series is generated from TPXO7.2 using the SLIM software [32] and computes the tidal currents using 13 tidal constituents. Since we only take into account the four main tidal constituents, this test also gives us an impression of the error we introduce by neglecting the other constituents.

The zonal and meridional velocities U and V caused by the tides are computed at the location 50°N, 25°W (in the North Atlantic) for one month, starting on January 1, 2002. The resulting time series are shown in Figure 5. The reference time series and the test series are plotted together to visualise the differences. For both the zonal and the meridional velocity, a zoom-in of a three-day interval is also shown, from which we can see that the phases of the test series and the reference series match. We notice a difference in amplitude, however. Since the nodal modulation amplitudes of the M_2, K_1 and O_1 constituents vary only very slowly with time, and that of the S_1 constituent does not vary at all, it is highly unlikely that these differences are the result of different modelling of the time-dependence of the amplitude (see also Section 2). Instead, it seems that these differences are caused by the neglect of tidal constituents other than M_2, S_2, K_1 and O_1 in our own run. To estimate the relative error, we compute the ratio of the mean absolute difference in velocity for both models and the maximum velocity value of our own test series. This ratio is approximately 11% for the zonal velocity and 7% for the meridional velocity.

A nice observation from our own time series is the spring-neap cycle caused by the M_2 and S_2 constituents (see Section 2.3). Indeed, we observe two spring currents and two neap currents in the 30-day period, and a little over 7 days between consecutive spring and neap currents. We can check if these occur at the correct times by checking the phases of the Moon; spring currents usually occur about two days after new and full moon (when the Sun and Moon are aligned), whereas neap currents arise a day or two after the first and last quarter (when there is a right angle between the Sun and Moon, and half the Moon is visible) [16]. In January 2002, new moon and full moon occurred on the 13th and 28th, respectively; the last and first quarter were on the 6th and 21st [31]. These dates are also marked in Figure 5. We see that the spring and neap currents in our time series indeed occur around the expected times.

3.4.2 Particle advection test

To compare the influence of advection by tidal currents to that by geostrophic and Ekman currents for a short timescale, a test run is carried out where we advect a single particle. We do this for two different cases: once in the open ocean, and once in a coastal area. For both situations, we release the particle on

[4] The criterion used to determine if a particle has beached is that its two last saved longitudes and latitudes are equal; in other words, the particle has been at the same position for the last four days of the run.

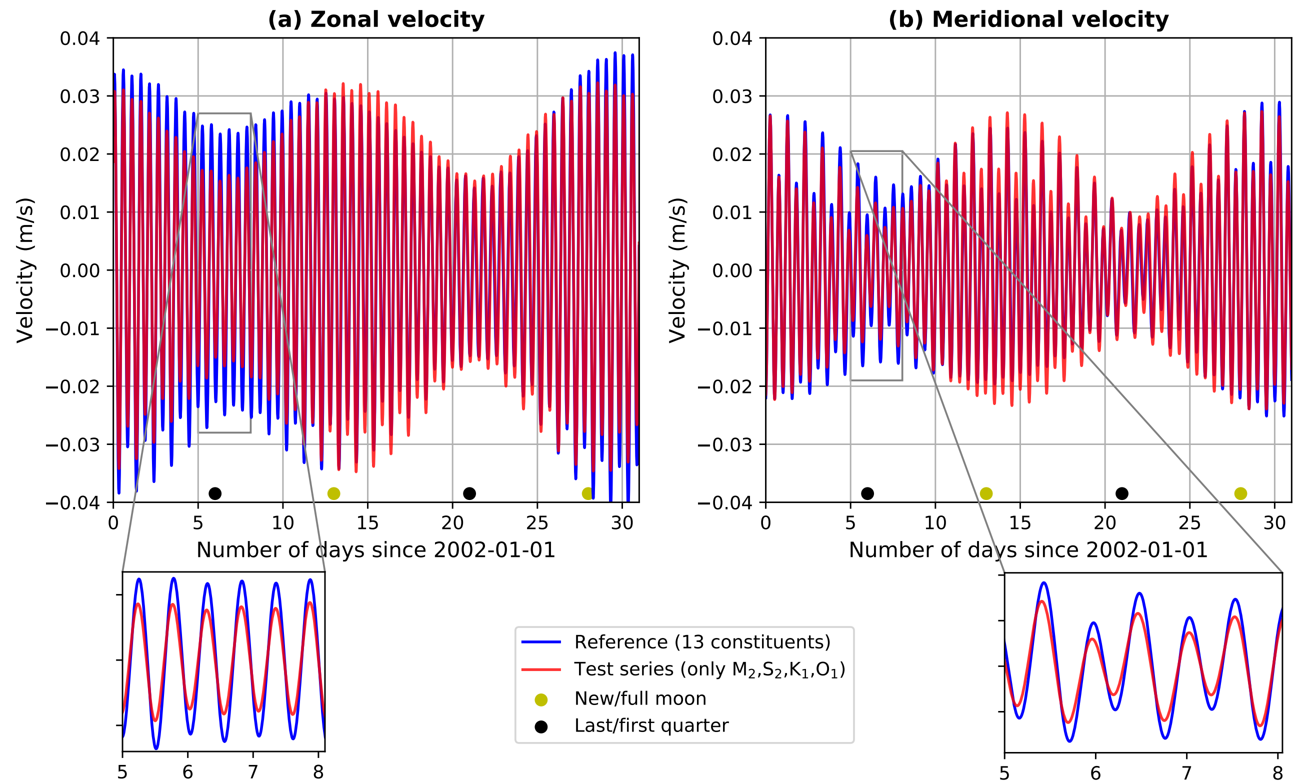

Figure 5: Time series for the zonal and meridional velocities caused by tides at location 50°N, 25°W for the month January 2002. The blue lines show the reference time series, generated from TPXO7.2 using the SLIM software, using data for 13 tidal constituents. The red lines show the time series generated from FES2014 using our own code, which only takes into account the M_2, S_2, K_1 and O_1 constituents. These red lines are slightly transparent so that overlap between the red and blue lines is clearly visible. The days when the Moon is new or full and the days when the Moon is in its last or first quarter are marked by yellow and black dots, respectively.

January 1, 2002, and advect it for 30 days with time step $\Delta t = 10$ minutes, with particle positions saved for every 30 minutes.[5] We do a GC run, FES run and GC+FES run.

In the first case, our particle is released at 50°N, 25°W, in the North Atlantic. The results for the FES run are shown in Figure 6. This figure shows the latitude and longitude of the particle as a function of time. We observe the oscillatory motion that we would expect from tidal currents, as well as the spring-neap cycle. Note that the differences in latitude and longitude over the course of the run are very small (both in the order of 0.001°, which corresponds to an order of 10^2 m). Moreover, both the latitude and longitude seem to oscillate around an equilibrium value, so that the particle keeps returning to (approximately) the same position.

The results from the three different runs are shown together in Figure 7. Here we see that the plots for the GC run and the GC+FES run are virtually indistinguishable. Moreover, the temporal variations caused by only the tidal currents are not even visible on the scale of the variations caused by all the surface currents. This strengthens our hypothesis that the influence of the tides on particle advection will be negligible in the open ocean.

[5] The time step as well as the time interval for saving the particle positions are made smaller in the test runs than in the final runs. This is done because the test runs are a lot shorter than the final runs. Saving data every two days when the run itself is only 30 days would yield very inaccurate results, so instead, it is saved every 30 minutes. The time step is made a bit smaller (10 minutes instead of 30 minutes) to further increase precision of the results, which we can afford without many extra computational costs because the test runs are relatively short already.

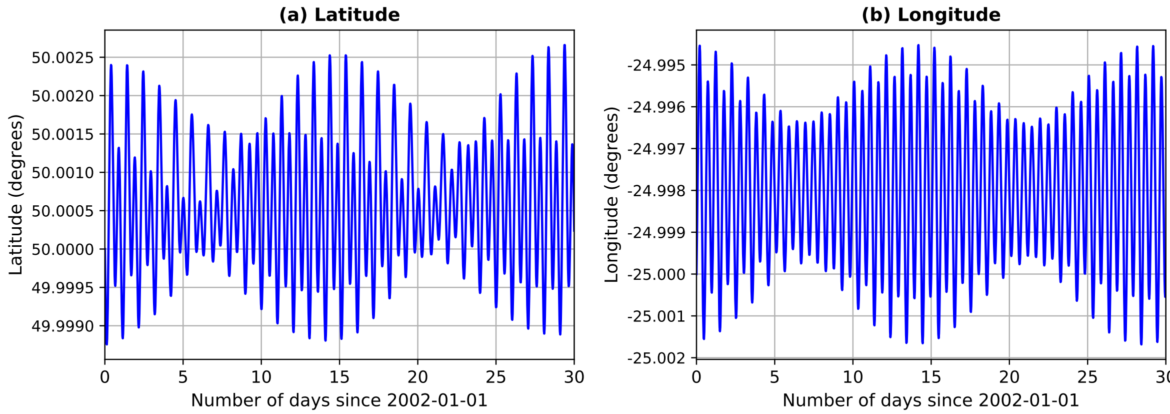

Figure 6: The latitude and longitude as a function of time of a particle released at 50°N, 25°W on 2002-01-01 and advected by the main tidal currents.

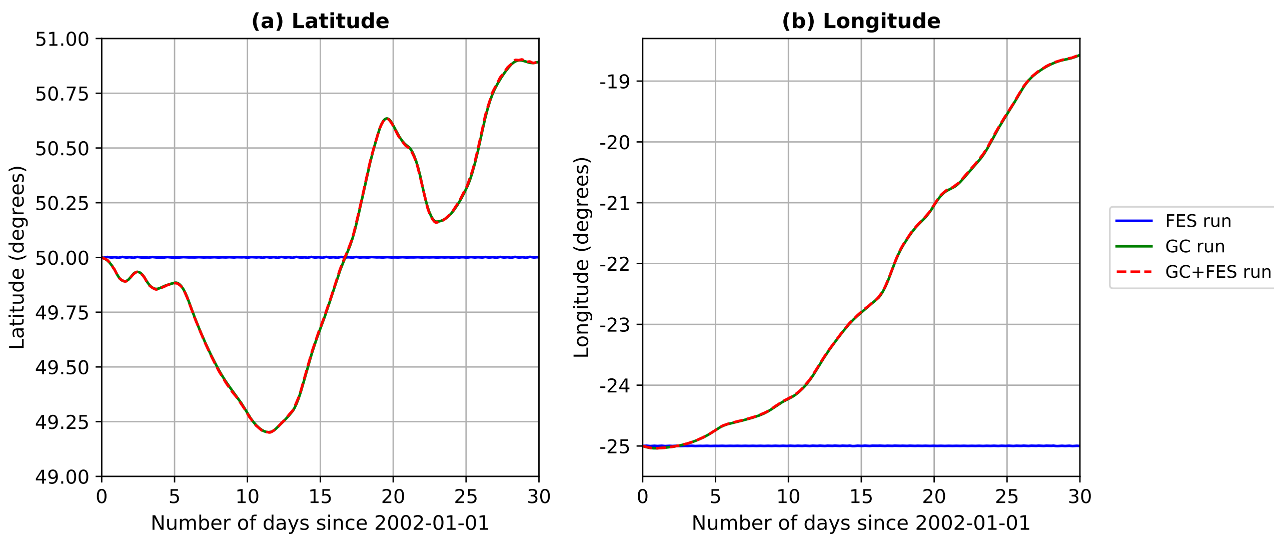

Figure 7: The latitude and longitude as a function of time of a particle released at 50°N, 25°W on 2002-01-01 and advected by the main tidal currents, geostrophic and Ekman currents, and the combination of these currents. Note that the green line (GC run) is beneath the dashed red line (GC+FES run).

In the second case, we release our particle at 52.5°N, 4.5°E; this is in the North Sea, near IJmuiden at the Dutch coast. The results we get here are very different from the previous case. Firstly, in Figure 8, the results from the FES run are shown. Note that the plots show a relatively large change in latitude and longitude of the particle during the first half day of the run; this is the result of the anti-beaching boundary current, which immediately pushes the particle away from the shoreline. After this, we again observe oscillatory motion, but now the particle also moves northward and a little eastward without returning to the same position after a certain amount of time. Comparing with Figure 8, we see that the changes in latitude and longitude of the particle when advected by only tidal currents are much larger in this coastal region than in the open ocean. The differences between the initial and final positions are now in the order of 10^4 m, as opposed to 10^2 m in the open ocean case (two orders of magnitude higher). Secondly, the results from all three runs are shown together in Figure 9. Now the effect of adding tidal currents to the geostrophic and Ekman currents is clearly visible. When the tidal currents are added, we see small oscillations appearing in the latitude and longitude as a function of time. The temporal variations caused by only tidal currents are still visible on this scale, and the plots showing the results from the GC run and from the GC+FES run show deviations in the order of 0.1° (order 10^4 m). Finally, let us consider the fate of the particle by looking at its *separation* after 30 days: the distance between the locations of the particle in the GC run and in the GC+FES run.[6] For the test near the coast, the separation is 5.0 km; by contrast, in the test in the open ocean, the separation is only 0.43 km, one order of magnitude less than in the coastal region.

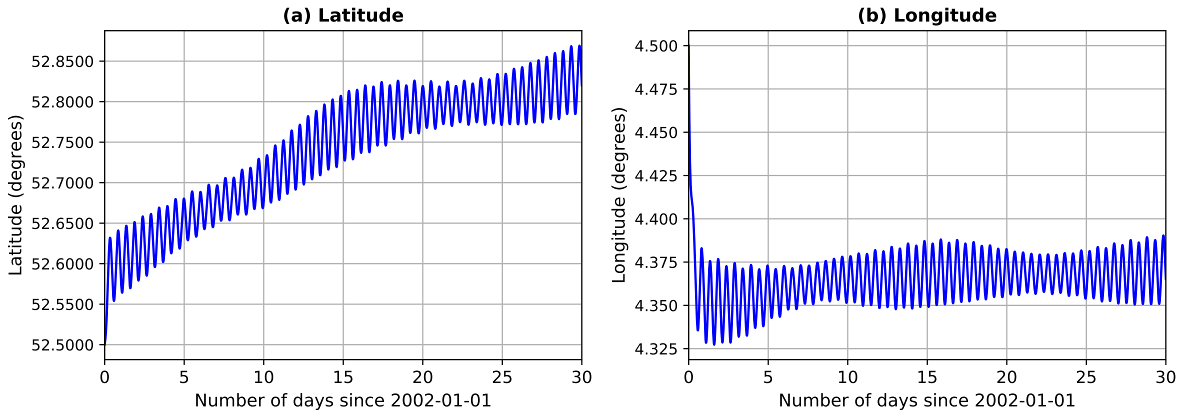

Figure 8: The latitude and longitude as a function of time of a particle released at 52.5°N, 4.5°E on 2002-01-01 and advected by the main tidal currents.

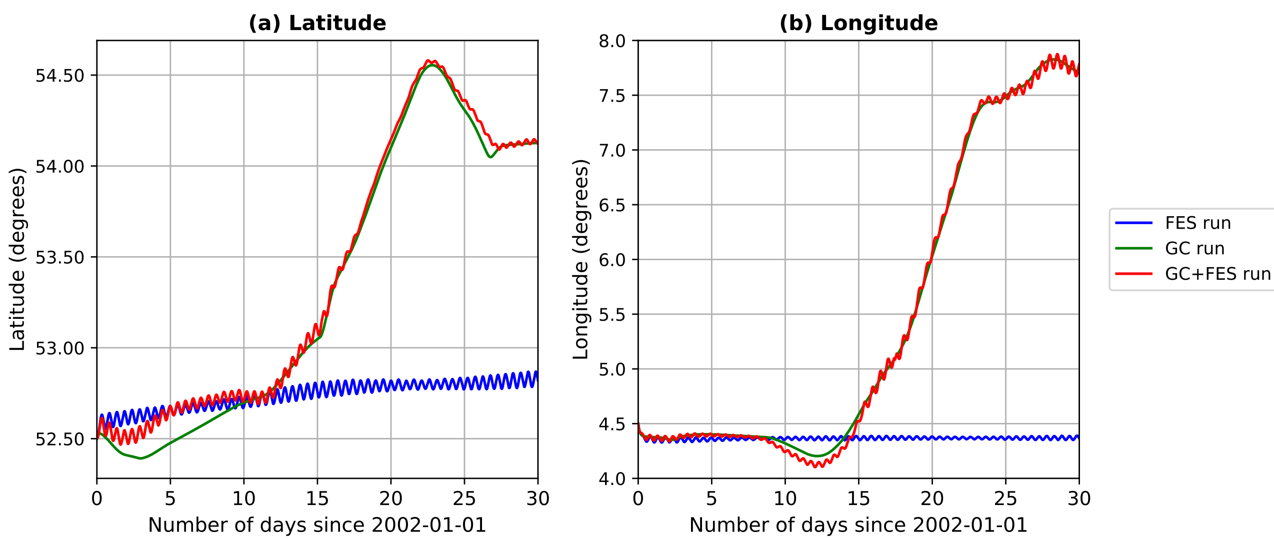

Figure 9: The latitude and longitude as a function of time of a particle released at 52.5°N, 4.5°E on 2002-01-01 and advected by the main tidal currents, geostrophic and Ekman currents.

The results of these test runs underline both the much higher relative importance of geostrophic and Ekman currents compared to tidal currents in particle advection, as well as the higher relative importance of tidal currents in coastal areas compared to regions in the open ocean. Note that these results are in line with our observations concerning the order of magnitude of tidal currents and geostrophic and Ekman currents (see Section 3.2). The order of magnitude of the tidal amplitudes in coastal areas is much larger than in the open ocean, and in most areas, the magnitude of these amplitudes is much smaller than that of the geostrophic and Ekman currents (see Figures 2, 3 and 4). This motivates our expectation that the influence of the tides on the pathways and fate of microplastic will be highest in coastal regions, but will in general be small.

[6] The distance between two particle locations is calculated as the great-circle distance; see Section 4.3 for more information.

4 Results

4.1 Particle density

To study the fate of microplastic in our runs, we investigate the density of plastic in the global ocean and how it changes in time (recall that the microplastic particles were initially uniformly distributed). We do this by dividing the global grid into bins of $1^{\circ} \times 1^{\circ}$ and for each year calculating the mean number of particles per surface area in each bin. The results for the GC run and the GC+FES run are shown for four different years of the runs in Figure 10 (note the logarithmic scale). The spatial patterns for the two runs are very similar. For the years 2010 and 2014 (the 9^{th} and 13^{th} year of the runs, respectively), some differences can be seen. In both situations, we see the formation of garbage patches in the five subtropical gyres, which is in agreement with observations [5, 6, 7, 8, 9]. Furthermore, a smaller area of accumulation can be identified in the Bay of Bengal. An enlarged version of Figures 10d and 10h (the densities in the final year) can be found in Appendix B.1.

To investigate the discrepancy between the results of the runs with and without tides, we consider the density differences between these runs. We do this for both the GC+FES run and the GC+FES30 run. For the initial and the final year of the simulation (2002 and 2014, respectively), the year-averaged particle density per bin in the GC+FES run minus the average density in the GC run are shown in Figures 11a and 11b (note the different scales in the two panels). The GC+FES30 density minus the GC density for the initial and final year are shown in Figures 11c and 11d.

We first focus on the density differences between the GC+FES run and the GC run. In Figure 11a and 11b, red indicates that the density is higher when the main tidal currents are added, blue that it is higher without tides. An interesting observation is that no regions which are uniformly red or blue are observed in the initial year. In the final year, the density differences are zero in many regions. This can be explained by the observation that the majority of the regions with non-zero density differences are precisely the aforementioned accumulation areas; in the rest of the oceans, the microplastic particle density is close to zero for both the GC run and the GC+FES run (Figure 10). In the final year, the density differences are also larger than in the initial year (absolutely as well as relatively). An explanation for this could be that simply more time has passed until the final year, and during this time perturbations caused by the tides can have grown. Still, there is no clear structure observable in most regions. Relatively large density differences are observed in the garbage patches, but there is no clear pattern of parts of garbage patches having structurally a lower or higher density with or without tides. However, a number of uniformly coloured areas outside the large subtropical garbage patches can be identified: they are marked in Figure 12, an enlarged version of Figure 11b. In this figure, the scale of the density differences is larger than in Figure 11b: this is done so that we have a clearer overview of areas with large density differences relative to the density values themselves (Figures 10d and 10h). There are five 'blue areas' where the densities are lower in the GC+FES run than in the GC run, marked with black frames: the Gulf of Mexico, the Barents Sea, the Irish Sea, the northernmost part of the Bay of Bengal, and the South China Sea along the coast of Vietnam. Furthermore, five 'red areas' are marked with a green frame: the Baltic Sea between Denmark and Sweden, the Bay of Biscay, a small coastal part in the Gulf of Guinea stretching from Ghana to Nigeria, the Great Australian Bight, and a rather large area to the southeast of Africa, in the region of the Agulhas Current. Although some of these areas (Irish Sea, Baltic Sea, Bay of Biscay, South China Sea, Gulf of Guinea) are very small in terms of surface area, they are interesting because they are uniformly coloured and are surrounded by regions with zero differences (especially the Gulf of Guinea area: it is the only part of the large area between the North and South Atlantic garbage patches where the density differences are non-zero). The Agulhas Current region contains a few 'blue spots', but since it is such a large area (compared to the other uniformly coloured areas), the vast majority of it is red, and the density differences are relatively large, it is still marked as a 'red area'. For each of these blue and red areas, the differences between the two runs can also clearly be seen in Figures 10d and 10h (or see the enlarged version, Figure 17, in Appendix B.1).

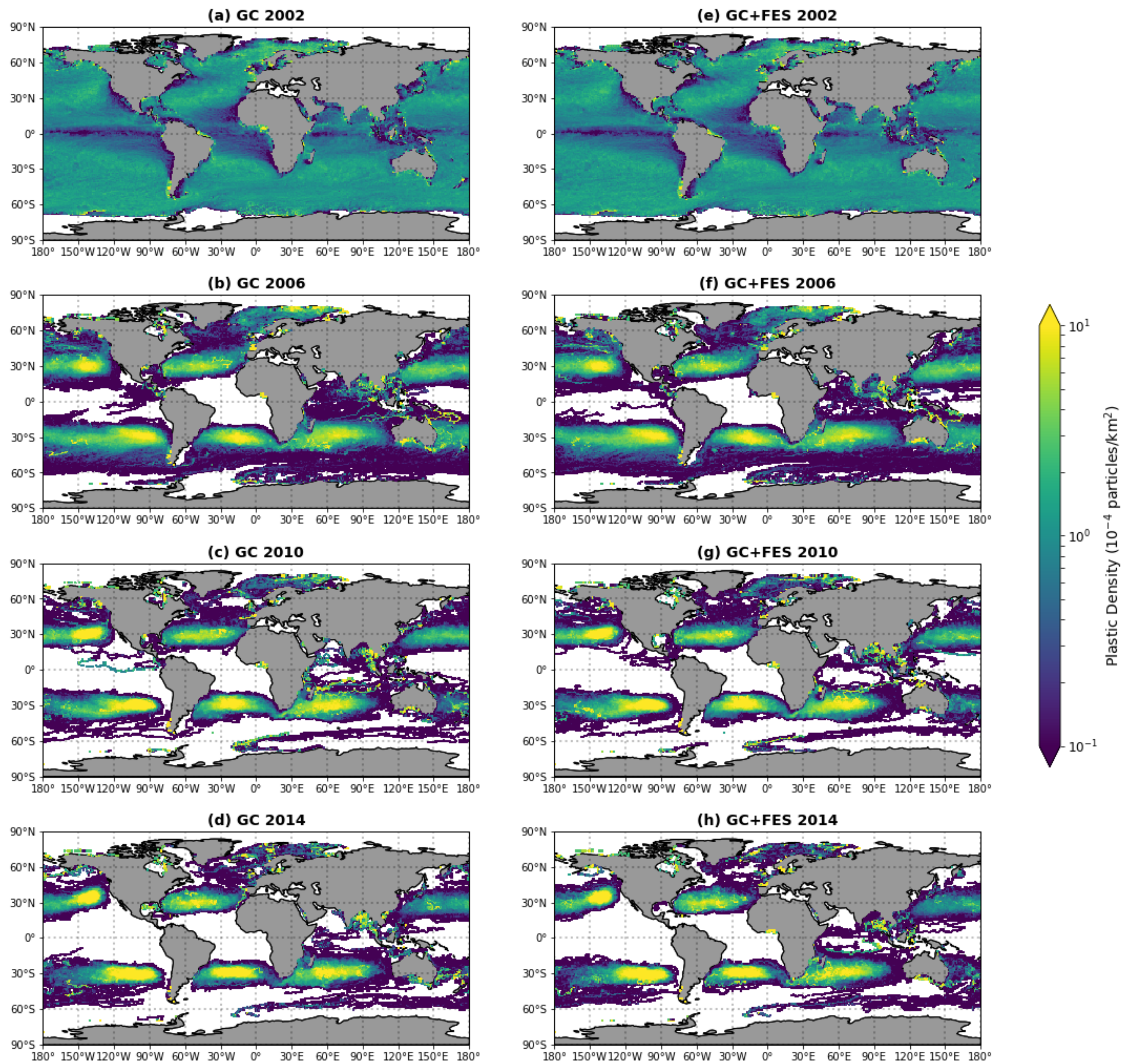

Figure 10: The average microplastic particle density for different years of the runs without tidal currents (left column) and with the main tidal currents (right column).

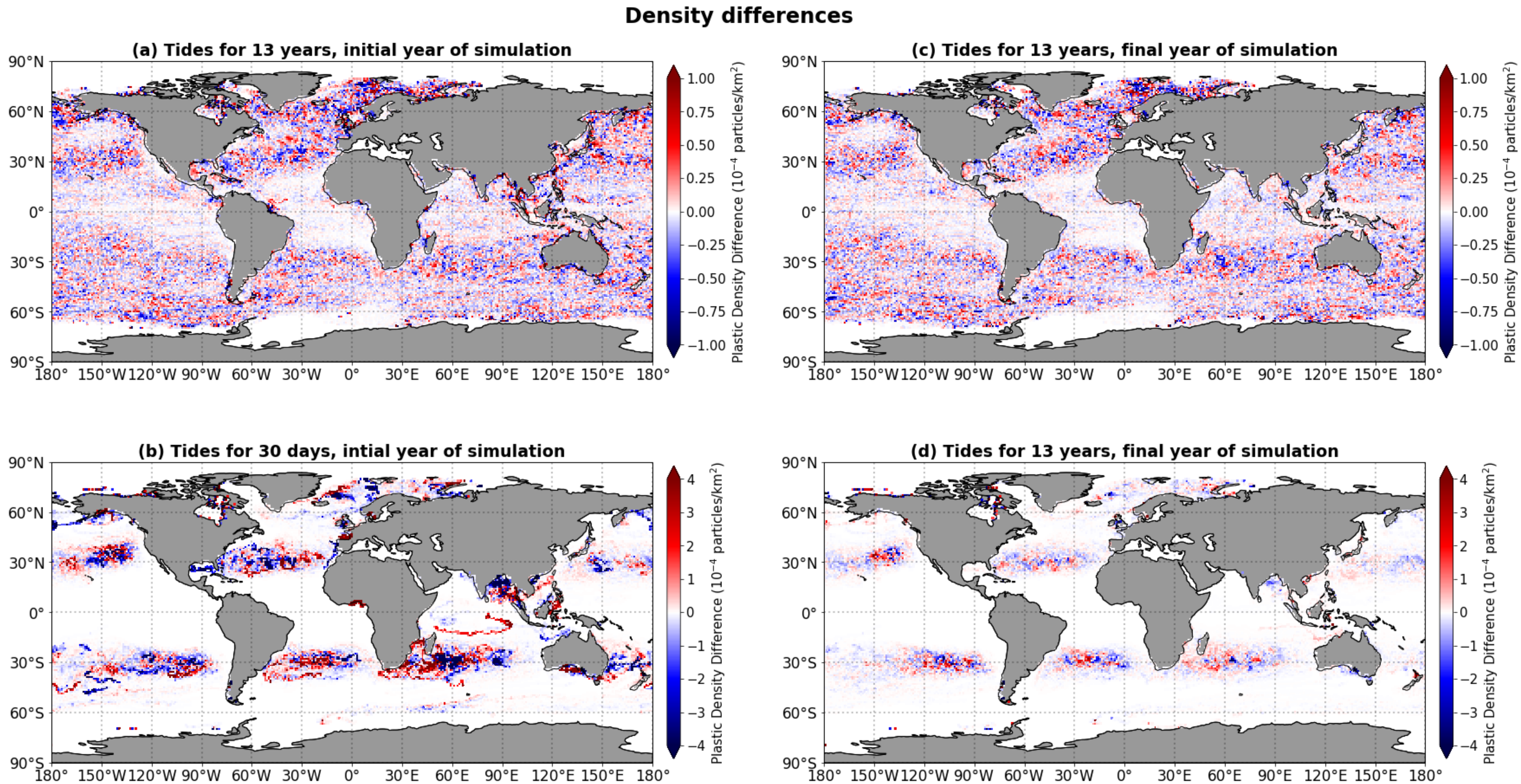

Figure 11: The average microplastic particle density in the run with the main tidal currents minus the average density in the run without tidal currents, for the initial and final year of the runs. Panels (a) and (b) show the results of the GC+FES run (tidal currents included during the entire run); panels (c) and (d) show the results of the GC+FES30 run (tidal currents modelled only for the first 30 days of the 13-year run).

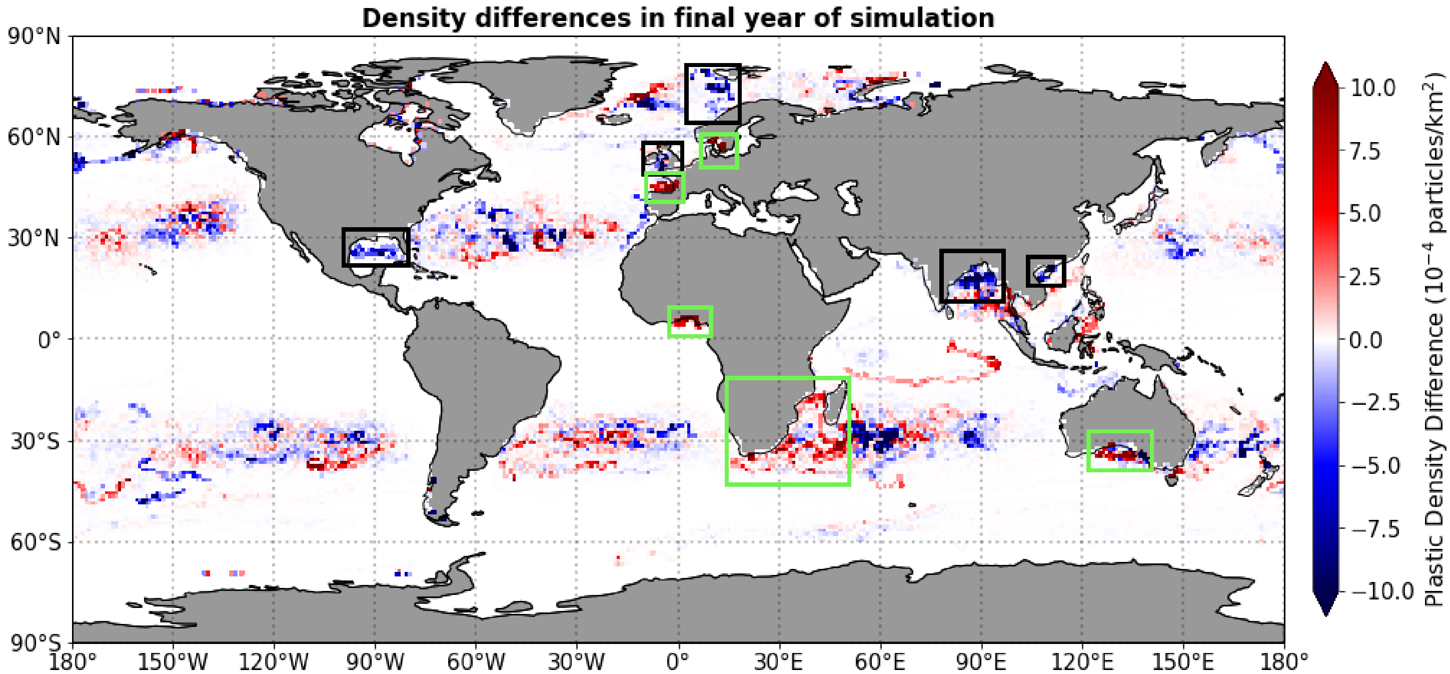

Figure 12: The average microplastic particle density in the GC+FES run minus the average density in the GC run for the final year of the runs. Regions where the density differences are almost uniformly negative are marked with black frames; regions where the differences are uniformly positive are marked with green frames.

Note that these blue and red areas are all near-coastal regions, though they are not necessarily the regions with the largest tidal velocity amplitudes (see Figures 3 and 4).

Apart from these regions, the density differences don't exhibit a clear spatial structure, but look very noisy. Moreover, the density differences seem to be almost evenly distributed around zero. We can check if the density difference distribution is indeed (approximately) symmetric around the mean by calculating its *skewness* γ_1, a measure of the asymmetry of a distribution [33]. For the initial year (Figure 11a), the skewness is approximately -10; the negative value indicates that the left tail of the difference distribution is more pronounced than the right tail, and the distribution is concentrated right of the mean. For the final year (Figure 11b), $\gamma_1 \approx 44$; now the right tail is longer and the difference distribution is concentrated on the left side. We can test if these values of the skewness are significant by computing their corresponding p-values, where we set our significance level $\alpha = 0.05$.[7] In both cases, the skewness has a p-value of 0.0, indicating that the skewness is significant and that the density differences are not symmetrically distributed around the mean. Since there is no clear spatial pattern in the differences, it is unclear what causes this skewness.

To test whether the observed spatial patterns in the density differences between the GC+FES run and the GC run are caused by the presence of tidal currents, we compare the results to the density differences between the GC+FES30 run and the GC run (Figures 11c and 11d). The spatial patterns for the initial year look very similar for both cases. For both runs, we see that in the final year the high values of density differences are concentrated in the garbage patches, and they are larger than in the initial year. However, in the GC+FES30 run the differences in the final year are smaller in magnitude than in the GC+FES run. Also, the areas with non-zero differences are smaller in the GC+FES30 run. This seems likely because in

[7] The p-value of the skewness γ_1 of a distribution gives the probability that if the distribution is symmetric around the mean (normally distributed), the skewness is (in absolute value) greater than or equal to $|\gamma_1|$. If this probability p is smaller than the significance level α, the skewness is significant, and the distribution is not symmetric.

this case, tidal currents are only present for less than 1% of the time, whereas in the GC+FES run they keep altering the particle's pathways and fate during the entire 13 years. An interesting observation is that the aforementioned uniformly blue and red areas in the final year (Figure 12) are only observed in the GC+FES run, and not in the GC+FES30 run (Figure 11d); the patterns in the GC+FES30 run look, as was expected, like random noise. This suggests that the blue and red areas in Figure 12 are in fact a result of advection by the main tidal currents.

As a measure of the relative differences, we divide the mean absolute density difference between the GC+FES run and the GC run by the mean density in the GC run. In other words, if we let $\mu(X)$ denote the mean of a distribution X and let ρ denote the microplastic particle density, we calculate

$$\text{relative density difference} = \frac{\mu\left(\left|\rho_{\text{GC+FES}} - \rho_{\text{GC}}\right|\right)}{\mu\left(\rho_{\text{GC}}\right)}.$$

For the initial year, this fraction is approximately 0.133; for the final year, it is 0.502. (We obtain the same (rounded) numbers when dividing by $\mu\left(\rho_{\text{GC+FES}}\right)$ instead.) So the mean absolute density differences are one order of magnitude smaller than the mean density itself. By comparison, for the GC+FES30 run, the relative differences are 0.114 for the initial year and 0.108 for the final year.

4.2 Distance travelled by particles

During the 13 years of the runs, the distance travelled by the particles since the beginning of the runs are tracked. Figure 13 shows the distance travelled at the end of the run as a function of the particle release location, for the three different runs. In Figure 13a, we see that in the FES run, there is a clear discrepancy between coastal regions and areas in the open ocean. There are a few coastal regions where the particles that start there travel relatively far; 10^5 km, as opposed to 10^4 km in the open ocean (where the value of the distance travelled is also almost uniform). Looking at Figures 3 and 4, we observe that the regions where the particles travelled furthest in the FES run are precisely the areas where the main tidal currents have the highest amplitude (this is most clearly visible for the M_2 tide). These figures explain the observed pattern in Figure 13a: in regions where the tidal velocity amplitudes are higher, the tidal currents are stronger (Section 2.2), so the particles get displaced over a greater distance per time step. Figure 13b shows the results from the GC run. Here we immediately see that the particles have in general travelled further than in the FES run. This is as expected, since the magnitude of the geostrophic and Ekman currents are almost everywhere one or two orders of magnitude higher than the amplitudes of the tidal currents (Figures 2, 3 and 4). In the GC run, particles released between 30°S and 30°N travel relatively far, and particles that started in the Indian Ocean travel the furthest. Figure 13c, which shows the results from the GC+FES run, looks very similar to Figure 13b. Two notable differences are that particles released around the Equator near West Africa have travelled less far in the GC+FES run than in the GC run, and particles released west of Great-Britain have travelled further in the GC+FES run than in the GC run.

Again, we are interested in the differences in distance travelled between the GC run and the GC+FES run, and also in the differences between the GC run and the GC+FES30 run. The distances travelled in the GC+FES run or the GC+FES30 run minus the distances travelled in the GC run are shown in Figure 14 for different times after the start of the runs: after 3 months, after 1 year, and after 13 years (at the end of the runs). Note that the panels have different scales. Red points indicate that a particle released at that location travelled further in the run with the main tidal currents than in the run without tides, blue points that it travelled less far. After 3 months, a clear structure is visible: particles released in areas where the amplitudes of the main tidal currents are large (Figure 3 and 4) have travelled further in the GC+FES run and in the GC+FES30 run than in the GC run. There are only very few release locations where particles have travelled further in the GC run than in the other two runs, and they don't show a clear spatial structure. In most parts of the global ocean, the differences in distance travelled are approximately zero. So on this timescale, the tidal currents clearly influence the distance travelled by the microplastic

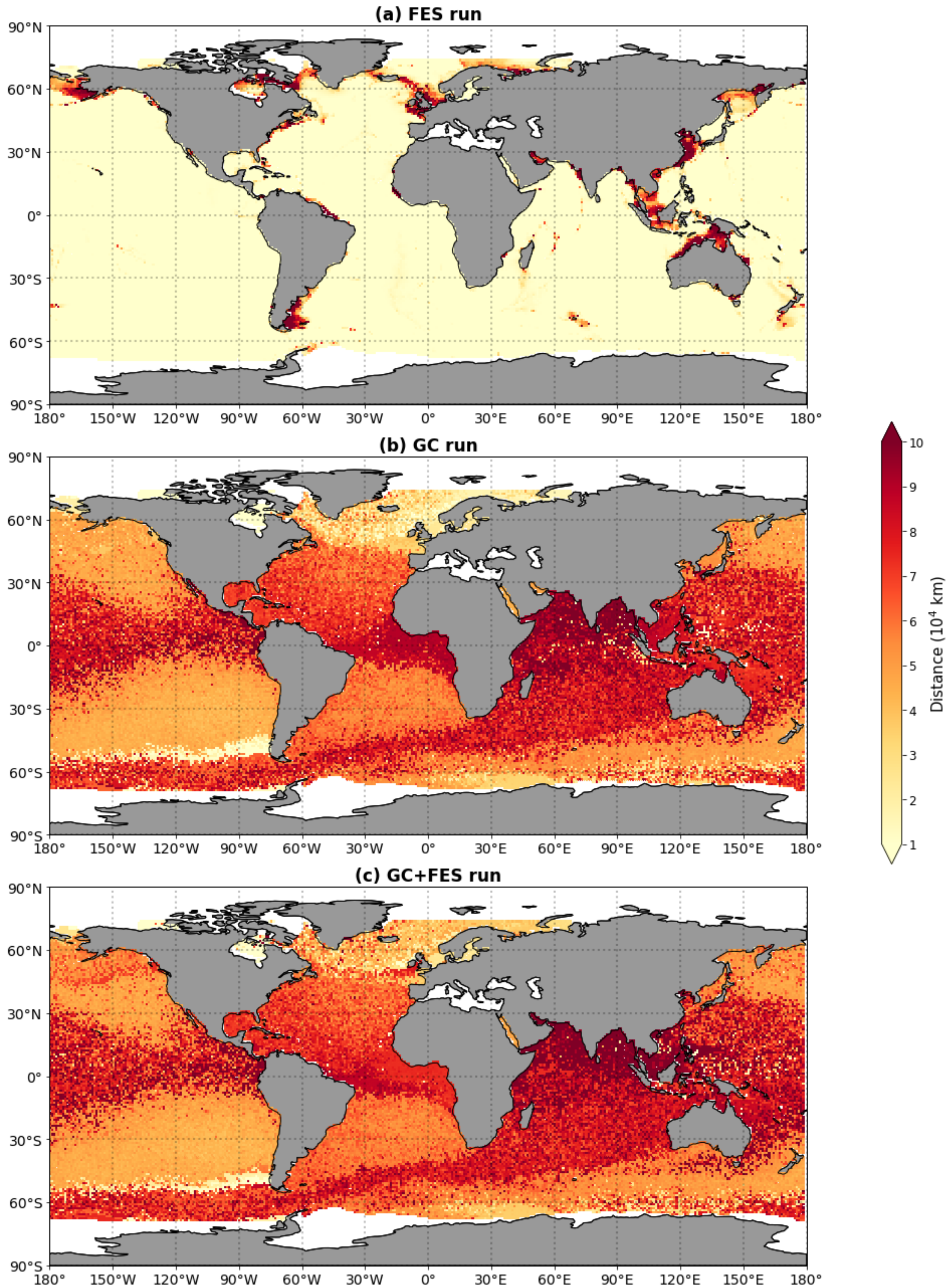

Figure 13: The distance travelled by particles at the end of the runs (i.e. after 13 years) for the three different runs, shown as a function of the particle release location.

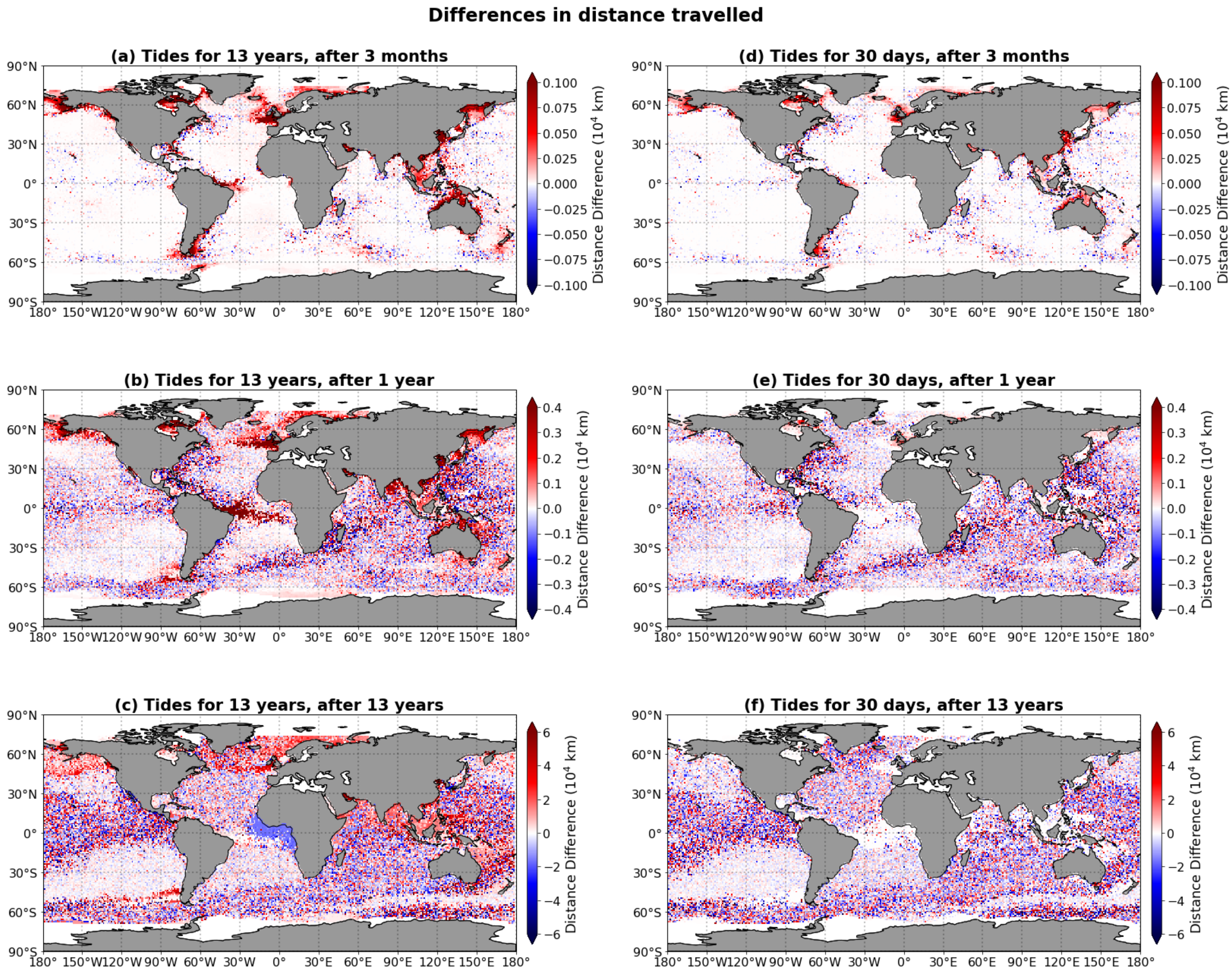

Figure 14: The distance travelled by particles in the run with the main tidal currents minus the distance travelled in the run without tidal currents, shown as a function of the release location, for different times after the start of the runs. Panels (a), (b) and (c) show the results of the GC+FES run (tidal currents included during the entire run); panels (d), (e) and (f) show the results of the GC+FES30 run (tidal currents modelled only for the first 30 days of the 13-year run).

particles released in coastal regions where the tidal amplitudes are high. A difference between the GC+FES run and the GC+FES30 run is that in the former, the differences in the areas with high amplitudes are in general larger than in the latter run, where tidal currents were only present for the first month. If we look at the differences in distance travelled after 1 year since the start of the runs, we see that there is still some spatial structure in case of the GC+FES run; the regions with large differences after 3 months are still present after 1 year. In the rest of the oceans, the differences are no longer zero, but noisy patterns form. Looking at the differences after 1 year for the GC+FES30 run, we see that the structures that were present after 3 months are now as good as lost, and the observed noisy patterns look the same as for the GC+FES run. After 13 years, there is not much structure left in the distance differences. The differences between the GC+FES run and the GC run show a few uniformly coloured areas; the band between 45°N and 75°N, the region along the southern and southeastern coast of Asia and a small region off the west coast of Chile are mostly red. In all these regions, the particles travelled further in the GC+FES run than in the GC run. Only one uniformly blue area can be identified, namely a rather large area in the Atlantic, along the west coast of Africa. Here particles travelled less far in the GC+FES run than in the GC run. None of these areas are observed for the GC+FES30 run; here, the differences look completely random after 13 years. Outside the uniformly coloured regions in Figure 13c, the spatial patterns look the same as in Figure 13f. It seems therefore that the uniformly red or blue areas form because of the main tidal currents, whereas the noisy patterns do not: they also develop if there has only been a short period of disturbance in the beginning of a run with only geostrophic and Ekman currents after these initial disturbances.

The mean values of the distance differences are shown in the first column of Table 2. For both runs, they are positive for all three times, and they increase with time. Furthermore, for all three times, the mean difference is smaller for the GC+FES30 run than for the GC+FES run. After 3 months, the mean differences have the same order of magnitude for both runs; after 1 year, the mean difference is one order of magnitude smaller in the GC+FES30 run than in the GC+FES run; after 13 years, it is two orders of magnitude smaller. As a measure of the relative differences, we divide the mean absolute difference in distance travelled after a certain amount of time by the mean distance travelled in the GC run at that time; that is, letting d denote distance travelled, we have

$$\text{relative difference in distance travelled} = \frac{\mu\left(|d_{\mathrm{GC+FES}} - d_{\mathrm{GC}}|\right)}{\mu\left(d_{\mathrm{GC}}\right)}.$$

The results are shown in the second column of Table 2. For each of the three times, the relative differences between the GC+FES30 run and the GC run are smaller than the relative differences between the GC+FES run and the GC run, although after 3 months and after 13 years, they have the same order of magnitude and the values are close to each other. For both runs, the mean absolute differences in distance travelled by the particles are initially two and later one order of magnitude lower than the mean distance travelled by particles in the GC run.

As a measure of the asymmetry of the distance difference distributions, we can calculate the skewness of the distributions. The results are shown in the third column of Table 2; the fourth column shows the corresponding p-values of the skewness. To test whether the skewness is significant, we use a significance level $\alpha = 0.05$. We see that the distance difference distributions are less skewed for the GC+FES30 run than for the GC+FES run at all three tested times. Moreover, for both runs, the skewness decreases with time. For the GC+FES run, the skewness is always positive, so the difference distribution always has a longer right tail. The p-value of the skewness is equal to zero in each case, so the skewness is significant and the differences are not symmetrically distributed. For the GC+FES30 run, the skewness is positive after 3 months and after 13 years, but negative after 1 year; here it is also very small. The p-value of the skewness is negligibly small after 3 months and after 13 years, so again, the differences are not symmetrically distributed around the mean. However, after 1 year, the skewness is approximately 0.34, which is larger than α. Hence, this skewness is not significant, and so the distance differences are symmetrically distributed around the mean value of 18 km (note that this value is very small on the scale of the distance differences in Figure 14f).

	Mean differences	**Relative differences**	**Skewness**	**Skewness p-value**
GC+FES, 3 months	55 km	0.053	8.5	0.0
GC+FES, 1 year	320 km	0.14	2.5	0.0
GC+FES, 13 years	2978 km	0.20	0.55	0.0
GC+FES30, 3 months	17 km	0.028	3.7	0.0
GC+FES30, 1 year	18 km	0.093	−0.013	0.34
GC+FES30, 13 years	69 km	0.15	0.11	$9.5 \cdot 10^{-16}$

Table 2: Data concerning the differences in distance travelled between the GC+FES run and the GC run and between GC+FES30 run and the GC run, for different times after the start of the runs. The first column shows the mean differences in distance travelled. The second column shows the mean absolute difference in distance travelled divided by the mean distance travelled in the GC run. The third column shows the skewness of the distribution of the distance differences, and the fourth column shows the corresponding p-value of the skewness.

4.3 Separation between particles

Consider pairs of particles in the run with tides and the run without tides that were released at the same location. The *separation* of this pair after a certain amount of time is the distance between the locations of the particles in the two different runs at that time. As a means to investigate the pathways of microplastic particles advected with or without tidal currents, we look at the separation of particle pairs in the GC run and the GC+FES run, and also at the separation in the GC run and the GC+FES30 run. The separation is calculated as the *great-circle distance*: presuming a spherical Earth with radius $a = 6371$ km, this is the shortest distance between two points on the Earth's surface, measured along the surface. The separation s between two points with latitudes ϕ_1, ϕ_2 and longitudes λ_1, λ_2 can be calculated as the great-circle distance using the *Haversine formula* [34]:

$$s = 2a \arcsin\left(\sqrt{\sin^2\left(\frac{\phi_2 - \phi_1}{2}\right) + \cos(\phi_1)\cos(\phi_2)\sin^2\left(\frac{\lambda_2 - \lambda_1}{2}\right)}\right). \tag{17}$$

The separation is plotted as a function of release location of the particle pairs in Figure 15, at 3 months, 1 year, and 13 years after the beginning of the runs. Note the different scales of the panels. After 3 months, no clear structure is visible. In the plots showing the results after 1 year and after 13 years, we observe that the patterns are similar to those observed in the differences in distance travelled (Figure 14): the areas with the largest separations largely correspond to the regions with large absolute differences in distance travelled between the two runs. The separations are in general smaller than the differences in distance travelled. This can be explained by considering the effect of advection by tidal currents: these currents are periodic, so they cause oscillatory motion of particles. With every oscillation, the distance a particle has travelled increases, but the particle has not necessarily moved far from its original location. A remarkable observation from Figure 15 is that at each time, the spatial structure for the GC+FES run and for the GC+FES30 run are very similar. One peculiar difference is that for the GC+FES30 run, there are more points where the separation is exactly zero (white points) than for the GC+FES run, for all three times. It is unclear what causes this. A possible explanation is the limited precision in the locations given by Parcels or rounding errors in calculating the distance between particle locations. Apart from this difference, there are two interesting regions where we see distinctions between the GC+FES run and the GC+FES30 run after 13 years: a region in Southeast Asia, surrounding Indonesia and the Philippines (largest separations in the Gulf of Thailand), and an area in the Atlantic, around the Equator near West Africa. In both regions, the separation is relatively large for the GC+FES run, but is zero or at least smaller for the GC+FES30 run. Both of these regions were also notable regions in the results of differences in distance travelled (Figure 14). In the region around Southeast Asia, particles had travelled further in the GC+FES run than in the GC run, whereas in this region west of Africa, particles had travelled less far in the GC+FES run than in

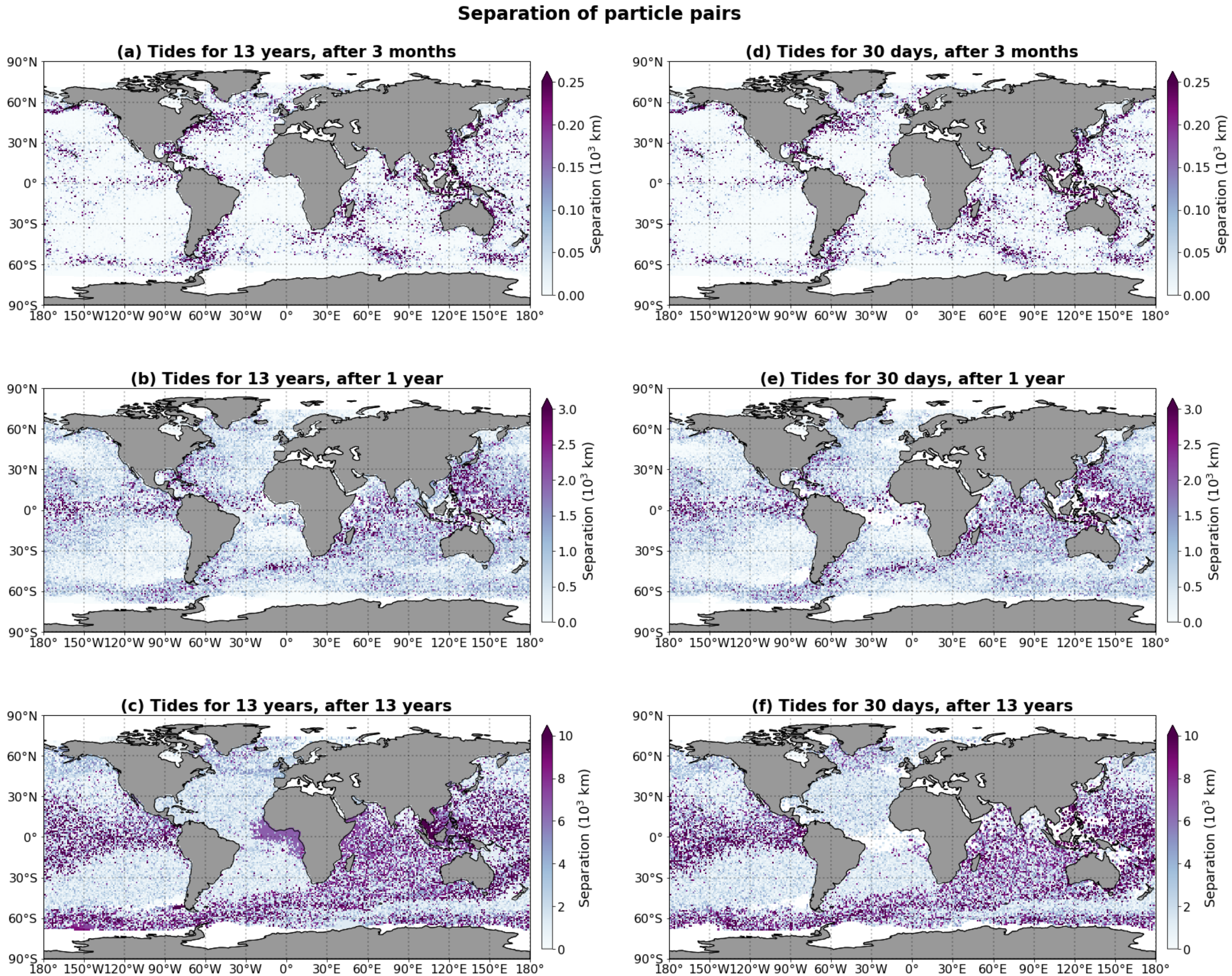

Figure 15: The separation between particles in the run with the main tidal currents and the run without tides, shown as a function of the release location, for different times after the start of the runs. Panels (a), (b) and (c) show the results of the GC+FES run (tidal currents included during the entire run); panels (d), (e) and (f) show the results of the GC+FES30 run (tidal currents modelled only for the first 30 days of the 13-year run).

the GC run (neither of these differences was observed for the GC+FES30 run). In all other regions, the patterns of the separation for the GC+FES run are noisy and are virtually the same as for the GC+FES30 run. Therefore, it seems that the two regions which show large differences between the two runs are the result of the presence of the main tidal currents, but the rest of the noisy separation patterns are not.

The mean separations between particles in the GC+FES run or GC+FES30 run and the GC run are reported in Table 3. The first two columns show the mean separations for the GC+FES run and the GC+FES30 run, respectively; the last column shows the ratio of these two (mean separation GC+FES divided by mean separation GC+FES30). We see that not only the mean separations themselves, but also the ratio of the GC+FES and GC+FES30 separations increases with time. After 3 months and after 1 year, the mean separation is approximately 10% larger in the GC+FES run than in the GC+FES30 run; after 13 years, this percentage has increased to almost 20%.

Mean separation	**GC+FES**	**GC+FES30**	$\frac{\textbf{GC+FES}}{\textbf{GC+FES30}}$
3 months	45 km	42 km	1.074
1 year	702 km	650 km	1.079
13 years	3584 km	3031 km	1.182

Table 3: Data concerning the mean separation between particles in the run with the main tidal currents and the run without tides, for different times after the start of the runs. The first column shows the mean separation between particles in the GC+FES run and the GC run. The second column shows the mean separation between particles in the GC+FES30 run and the GC run. The third column shows the ratio of the first and second column.

Finally, it is interesting to consider the mean separation (averaged over all particle pairs) of the GC+FES run as a function of time. This is shown as a log-log plot in Figure 16. The mean separation increases with time, as we would expect because disturbances can grow with time, and tidal currents can alter the pathways of microplastic particles during the entire run. There exist theories that predict three distinct regimes in this plot [35].[8] Indeed, it seems that three different regimes can be discerned in Figure 16. The graph, which is increasing at all times, is first concave up for a while; then it becomes steeper, while remaining concave up; and finally, it becomes concave down. The study of these results and comparison with other studies is beyond the scope of this project, and for further information, we refer to e.g. [35] and [36].

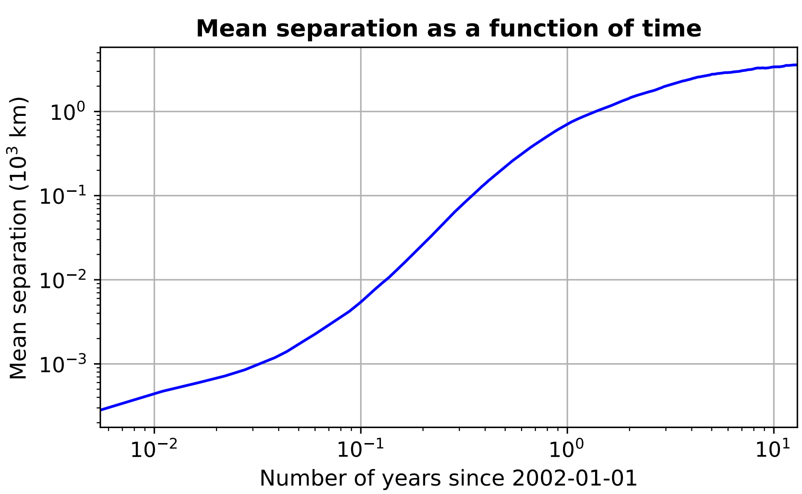

Figure 16: The mean separation of all particle pairs released in the GC run and the GC+FES run as a function of time.

[8]However, experimental results are often different from the theory and also from each other.

5 Discussion and conclusion

5.1 Uncertainties and errors

A number of uncertainties in the model used for the runs in this project require discussion. First of all, an error is introduced in our runs by taking only the M_2, S_2, K_1 and O_1 currents into account in the model of tidal currents. By doing this, we neglect the numerous other tidal constituents that could influence the outcomes of the runs. We saw in our time series test run, described in Section 3.4.1, that relative errors of approximately 10% in the velocity magnitude occurred between time series generated using only the main tidal constituents and time series where 13 different tidal constituents were used. We should therefore be careful in drawing quantitative conclusions from our runs. Nevertheless, it is reasonable to assume that our qualitative conclusions about the influence of tidal currents on transport of microplastic are robust, and that adding more tidal constituents, which have smaller velocity amplitudes than the four constituents already included, would not alter these conclusions drastically.

Secondly, recent studies [37, 38] showed that the GlobCurrent dataset agrees better with observations in the open ocean than in coastal regions; the spatial resolution is too coarse in coastal regions to yield accurate estimates of coastal currents. In particular, it seems that more work is required to find accurate estimates of the surface currents in areas where the tides are strong [37]. Coastal areas with large tidal currents are precisely the areas that this project has identified to be interesting, so it should be noted that the data for the geostrophic and Ekman currents from GlobCurrent may not be entirely accurate in these regions.

Another source of uncertainty in the outcomes of the runs is the possibly incomplete modelling of the physical processing determining microplastic transport. For example, the model used in this study does not take into account the possibility for particle beaching. Moreover, the flows in the model are two-dimensional, so particles cannot sink to deeper ocean layers. These model inaccuracies can produce results that are not entirely realistic. Nonetheless, the aim of this project is not to compare the outcomes with observational data, but merely to determine whether tidal currents play a relevant role in the transport of floating microplastic in oceans.

Finally, uncertainties and errors in the results might occur due to computational (rounding) errors and the limited precision of the numerical methods used. For example, the accuracy of the computation of particle trajectories could be increased by using a numerical method which is more accurate than RK4, or by making the time step in the runs smaller (see Section 3.3). Another example is that the accuracy of the results of the particle density (Section 4.1) could be increased by making the bins in which we calculate the density smaller. Moreover, it should be noted that the size of the bins is not constant over the Earth. We have taken bins of $1^\circ \times 1^\circ$, and the length of 1° longitude varies with latitude, so that the bins around the Equator are larger than those at higher or lower latitudes; thus the particle densities are not calculated over constant surface areas.

5.2 Conclusions

The results from our runs show a number of differences caused by the main tidal currents in the pathways and distribution of microplastics, almost all of which occur in (near-)coastal regions. First of all, we study the fate of microplastic by considering the plastic particle density distribution across the global ocean after different amounts of time since the start of the runs. Here we find no clear effects on a short timescale (after 1 year). On a longer timescale, we observe that the formation of garbage patches remains virtually unchanged when the main tidal currents are added in the run, though relatively large density differences compared to the run without tides can be seen in some areas of the garbage patches. These areas with non-zero differences are also observed in the differences between the GC+FES30 run and the GC run, though there the differences are smaller in magnitude. The relative differences in this final year of the simulations are approximately 50% for the GC+FES run, and only about 10% for the GC+FES30 run. In this final year, some striking regions outside the garbage patches with relatively large density differences can be distinguished for the GC+FES run that are not present in the GC+FES30 run. All of these regions are (near-)coastal areas where the particle densities over the whole area are either larger or smaller in the GC+FES run than in the GC run. It should be noted that almost all of these regions have a small surface area (compared to e.g. the garbage patches). There is, however, one relatively large region to the southeast of Africa, in the region of the Agulhas Current; here, the particle densities are larger in the GC+FES run than in the GC run. In all of these regions, the density differences between the two runs are in the order of 10^{-3} particles/km^2, which is the same order of magnitude as the densities found there in the GC run. The fact that none of these areas are observed in the GC+FES30 run suggests that they are not the random results of small disturbances on a long timescale, but are the result of advection of microplastic particles by the main tidal currents.

Next, we also investigate how the pathways of microplastics are influenced by the main tidal currents. For this, we first consider the distance that particles have travelled after certain amounts of time. On a short timescale (3 months) we can see very clearly that particles released in coastal regions travel greater distances when the main tidal currents are included than when they are not. As time passes, this structure gets lost, and after 13 years almost all of the patterns observed in the differences in distance travelled between the GC+FES run and the GC run look like random noise (the same patterns are observed in the differences between the GC+FES30 run and the GC run). However, there are again a few areas where we clearly see larger differences in the GC+FES run than in the GC+FES30 run. In almost the entire band between 45°N and 75°N, particles that are released there have travelled further in 13 years in the GC+FES run than in the GC run; the same is true for the southern and southeastern coastal regions of Asia and a small region near Chile. There is also a relatively large area west of Africa where released particles travel less far with the main tidal currents than without them. The relative differences in distance travelled between the GC+FES run and the GC run after 13 years are approximately 20%; between the GC+FES30 run and the GC run, they are 15%. These numbers are close together, although relative differences are higher for the GC+FES run than for the GC+FES30 run, which is caused by the aforementioned regions with large differences.

In addition, for studying the pathways of microplastics, it is interesting to consider the separation between particle pairs released at the same location in a run with the main tidal currents and the run without tidal currents. No clear patterns are observed for the separations on a short timescale (after 3 months or after 1 year). After 13 years, we see that in the sea around Southeast Asia and an area west of Africa (the same regions that were just mentioned in the context of distance travelled), the separations are larger for the GC+FES run than for the GC+FES30 run; they are largest for Southeast Asia. In the rest of the oceans, patterns are the same for both runs and can therefore be considered random. The mean separation of particle pairs is approximately 20% larger in the GC+FES run than in the GC+FES30 run at the end of the simulations.

All these results show that the formation of the garbage patches in the five subtropical gyres remains unaffected by the addition of the main tidal currents. However, comparisons between the GC+FES run and the GC+FES30 run (where random patterns are expected) show that there are a number of regions where the main tidal currents have a clear influence on the distance that floating microplastic particles can travel (on short as well as long timescales) and on the regions where they end up. All of the regions where significant differences are observed between the run with the main tidal currents and the one without tides are (near-)coastal regions. These results suggest that tidal currents are of negligible relevance to the transport and accumulation of floating marine microplastic in the open ocean on a global scale, but can be useful to include in simulations and research focused on the pathways and fate of microplastic particles in coastal environments.

5.3 Future work

A suggestion for interesting future research would be to repeat the simulations from this project with more tidal constituents added. As discussed in Section 5.1, the neglect of constituents other than the main constituents M_2, S_2, K_1 and O_1 in the calculation of tidal currents introduces an error in the results of the simulations. Addition of more tidal constituents would enable us to see how large this error is, and investigate if the pathways and fate of microplastics in the ocean are significantly influenced by tidal currents other than the main tidal currents. Data for more constituents is available in the TPXO7.2 and FES2014 datasets: the TPXO7.2 dataset contains 13 different tidal constituents [27] and the FES2014 dataset contains 34 [28]. Information and formulas for the computation of the nodal modulation amplitude and phase corrections and the astronomical argument correction for the different tidal constituents can be found in Schureman (1958) [19] and in the code accompanying the FES2014 dataset [28]. Additionally, it would be worth considering to use a different dataset than GlobCurrent for the geostrophic and Ekman surface currents because GlobCurrent is less accurate in coastal regions with strong tidal currents than in the open ocean (see Section 5.1). Finally, it would be useful to include a model and data for wind (especially strong storms) and its interaction with tidal currents, because wind can influence the magnitude of the tides [15, 18].

As for the results of this project, there are a number of things that would be interesting to investigate further. We could, for example, study the connectivity of ocean basins: that is, we could look at the percentage of particles released in one basin that end up in another basin. This could help us gain more insight into the pathways of the modelled microplastic particles, and maybe find connections between the results for particle density (Section 4.1) and pairwise separation (Section 4.3). Another result that would require more in-depth study is the mean separation of particle pairs advected with and without the main tidal currents as a function of time. When we plot it on a log-log scale (Figure 16), we observe three different regimes. It would be interesting to compare this result with existing theories and experiments concerning these regimes.

The research focus of this project was the effect of tidal currents on *global* transport of microplastic in oceans. Since our findings are that effects are observable mainly in (near-)coastal regions, and the amplitudes of tidal current velocities are in general largest in such regions, it would be interesting to conduct further research that focuses on transport of microplastics in coastal areas. What should certainly be included in such research is a model for particle beaching, and a study of the influence of tidal currents on the probability that microplastic particles wash ashore. Moreover, it would be interesting to release particles only along shorelines, where the tidal currents are strongest. The transport and residence time of microplastics in coastal regions could be considerably influenced by strong tidal currents. An example of such influence is that stranded plastic particles can easily be washed back into sea during spring tides [10]. Furthermore, observations of floating plastic debris in the surface waters of the Tamar Estuary (UK) reported a significant difference in the plastic particle's size frequency distribution between the spring and neap tides; during spring tides, more fragments of larger size were observed [39]. Identifying and studying these influences of tidal currents explicitly could help us increase our understanding of the pathways and fate of microplastics in coastal environments.

Acknowledgements

First and foremost, I would like to thank my supervisor Dr. Erik van Sebille and my co-supervisor Dr. Philippe Delandmeter for their guidance, encouragement and advice throughout this project. They often provided me with great suggestions and were always willing to offer help when I had no idea where all the bugs in my code came from. I would also like to express my gratitude towards Prof. Huib de Swart, who greatly helped me in understanding the theory of harmonic analysis of the tides. Victor Onink also deserves thanks for providing me with example code for running global simulations using Parcels and for processing their results. Furthermore, I thank Dr. Andreas Sterl for his feedback on my report, and Dr. Mereke van Garderen and Florian Sterl for their advice on the layout and colormaps of my figures. I am very grateful to Caroline Sterl for making the beautiful painting on the title page of this thesis. Finally, I thank Dr. Philippe Delandmeter, David Wichmann and Peter Nooteboom for graciously allowing me to work in their office during this project.

The GlobCurrent v3 data can be found at `http://www.ifremer.fr/opendap/cerdap1/globcurrent/v3.0/`. The TPXO7.2 dataset can be found at `http://volkov.oce.orst.edu/tides/TPXO7.2.html`. The FES2014 can be accessed via `https://www.aviso.altimetry.fr/en/data/products/auxiliary-products/global-tide-fes.html` (subscription is required to get access). FES2014 was produced by Noveltis, Legos and CLS and distributed by Aviso+, with support from CNES (`https://www.aviso.altimetry.fr/`). The code used to compute FES2014, was developed in collaboration between Legos, Noveltis, CLS Space Oceanography Division and CNES is available under GNU General Public License.

References

[1] B.D. Hardesty, J. Harari, A. Isobe, L. Lebreton, N. Maximenko, J. Potemra, E. Van Sebille, A.D. Vethaak, & C. Wilcox (2017). *Using numerical model simulations to improve the understanding of micro-plastic distribution and pathways in the marine environment.* Frontiers in Marine Science, Vol. 4, No. 30, pp. 1-9.

[2] C.J. Moore (2008). *Synthetic polymers in the marine environment: A rapidly increasing, long-term threat.* Environmental Research, Vol. 108, pp. 131-139.

[3] J.R. Jambeck, R. Geyer, C. Wilcox, T.R. Siegler, M. Perryman, A. Andrady, R. Narayan, & K.L. Law (2015). *Plastic waste inputs from land into the ocean.* Science, Vol. 347, No. 6223, pp. 768-771.

[4] M. Eriksen, L.C.M. Lebreton, H.S. Carson, M. Thiel, C.J. Moore, J.C. Borerro, F. Galgani, P.G. Ryan, & J. Reisser (2014). *Plastic pollution in the world's oceans: More than 5 trillion plastic pieces weighing over 250,000 tons afloat at sea.* PLoS ONE, Vol. 9, No. 12, pp. 1-15.

[5] E. van Sebille, C. Wilcox, L. Lebreton, N. Maximenko, B.D. Hardesty, J.A. Van Franeker, M. Eriksen, D. Siegel, F. Galgani, & K.L. Law (2015). *A global inventory of small floating plastic debris.* Environmental Research Letters, Vol. 10, No. 12, pp. 1-11.

[6] A. Cózar, F. Echevarria, J.I. González-Gordillo, X. Irigoien, B. Ubeda, S. Hernandez-Leon, A.T. Palma, S. Navarro, J. Garcia-de-Lomas, A. Ruiz, M.L. Fernandez-de-Puelles, & C.M. Duarte (2014). *Plastic debris in the open ocean.* Proceedings of the National Academy of Sciences, Vol. 111, No. 28, pp. 10239-10244.

[7] L.C.-M. Lebreton, S.D. Greer, & J.C. Borrero (2012). *Numerical modelling of floating debris in the world's oceans.* Marine Pollution Bulletin, Vol. 64, pp. 653-661.

[8] N. Maximenko, J. Hafner, & P. Niiler (2012). *Pathways of marine debris derived from trajectories of Lagrangian drifters.* Marine Pollution Bulletin, Vol. 65, pp. 51-62.

[9] E. van Sebille, M.H. England, & G. Froyland (2012). *Origin, dynamics and evolution of ocean garbage patches from observed surface drifters.* Environmental Research Letters, Vol. 7, No. 4, pp. 1-6.

[10] H. Zhang (2017). *Transport of microplastics in coastal seas.* Estuarine, Coastal and Shelf Science, Vol. 199, pp. 74-86.

[11] M. Cole, P. Lindeque, C. Halsband, & T.S Galloway (2011). *Microplastics as contaminants in the marine environment: a review.* Marine Pollution Bulletin, Vol. 62, pp. 2588-2597.

[12] J.P.W. Desforges, M. Galbraith, N. Dangerfield, & P.S. Ross (2014). *Widespread distribution of microplastics in subsurface seawater in the NE Pacific Ocean.* Marine Pollution Bulletin, Vol. 79, pp. 94-99.

[13] H.S. Auta, C.U. Emenike, & S.H. Fauziah (2017). *Distribution and importance of microplastics in the marine environment: a review of the sources, fate, effects, and potential solutions.* Environment International, Vol. 102, pp. 165-176.

[14] J.R. Taylor (2005). *Classical Mechanics.* University Science Books, Mill Valley, California, ISBN 978-1-891389-22-1.

[15] The Open University (1999). *Waves, Tides and Shallow Water Processes*, second edition. Butterworth-Heinemann, Oxford.

[16] G. Godin (1972). *The Analysis of Tides.* Liverpool University Press, Liverpool, ISBN 0 85323 441 8.

[17] B. Cushman-Roisin & J.-M. Beckers (2011). *Introduction to Geophysical Fluid Dynamics*, second edition. Elsevier Science Publishing Co Inc, ISBN 978-0-12-088759-0.

[18] National Ocean Service, *Tides and Water Levels*, `https://oceanservice.noaa.gov/education/tutorial_tides/`. Last accessed 12-12-2018.

[19] P. Schureman (1958). *Manual of Harmonic Analysis and Prediction of Tides.* U.S. Department of Commerce, Coast and Geodetic Survey, Special Publication No. 98.

[20] M.G.G. Foreman & R.F. Henry (1989). *The harmonic analysis of tidal model time series.* Advances in Water Resources, Vol. 12, pp. 109-120.

[21] M.G.G. Foreman (1977). *Manual for Tidal Heights Analysis and Prediction.* Pacific Marine Science Report 77-10.

[22] A. T. Doodson (1921). *The Harmonic Development of the Tide-generating Potential.* Proceedings of the Royal Society, Series A, Vol. 100, No. 704, pp. 305-329.

[23] S. Casotto & F. Biscani (2004). *A fully analytical approach to the harmonic development of the tide-generating potential accounting for precession, nutation, and perturbations due to figure and planetary terms.* Bulletin of the American Astronomical Society, Vol. 36, p. 862.

[24] M.-H. Rio, J. Johannessen, & C. Donlan (2015). *Product data handbook: The combined Geostrophy +Ekman currents.*

[25] M.-H. Rio, S. Mulet, & N. Picot (2014). *Beyond GOCE for the ocean circulation estimate: Synergetic use of altimetry, gravimetry, and in situ data provides new insight into geostrophic and Ekman currents.* Geophysical Research Letters, Vol. 41, pp. 89188925.

[26] D.P. Dee, S.M. Uppala, A.J. Simmons, P. Berrisford, P. Poli, S. Kobayashi, U. Andrae, M.A. Balmaseda, G. Balsamo, P. Bauer, P. Bechtold, A.C.M. Beljaars, L. van de Berg, J. Bidlot, N. Bormann, C. Delsol, R. Dragani, M. Fuentes, A.J. Geer, L. Haimberger, S.B. Healy, H. Hersbach, E.V. Hólm, L. Isaksen, P. Kållberg, M. Köhler, M. Matricardi, A.P. McNally, B.M. Monge-Sanz, J.-J. Morcrette, B.-K. Park, C. Peubey, P. de Rosnay, C. Tavolato, J.-N. Thépaut, & F. Vitart (2011). *The ERA-Interim*

reanalysis: Configuration and performance of the data assimilation system. Quarterly Journal of the Royal Meteorological Society, Vol. 137, No. 656, pp. 553597.

[27] G.D. Egbert & S.Y. Erofeeva (2002). *Efficient inverse modeling of barotropic ocean tides.* Journal of Atmospheric and Oceanic Technology 19.2, pp. 183-204.

[28] L. Carrère, F. Lyard, M. Cancet, A. Guillot, N. Picot, & S. Dupuy (2015). *FES2014: A New Global Tidal Model* Presented at the Ocean Surface Topography Science Team Meeting, Reston, USA.

[29] M. Lange & E. Van Sebille (2017). *Parcels v0.9: prototyping a Lagrangian ocean analysis framework for the petascale age.* Geoscientific Model Development, Vol. 10, pp. 4175-4186.

[30] U.M. Ascher & C. Greif (2011). *A First Course in Numerical Methods.* Society for Industrial and Applied Mathematics, Philadelphia, ISBN 978-0-898719-97-0.

[31] Moon Phases January 2002, `https://www.calendar-12.com/moon_calendar/2002/january`. Last accessed 2018-11-28.

[32] SLIM: *a multi-scale model of the land-sea continuum*, `https://www.slim-ocean.be/`. Last accessed 2018-12-12.

[33] Eric W. Weisstein, *Skewness*. From *MathWorld*–A Wolfram Web Resource, `http://mathworld.wolfram.com/Skewness.html`. Last accessed 2018-12-20.

[34] R.W. Sinnott (1984). *Virtues of the Haversine*. Sky and Telescope, Vol. 68, No. 2, p. 159.

[35] J.H. LaCasce (2008). *Statistics from Lagrangian observations*. Progress in Oceanography, Vol. 77, No. 1, pp. 1-29.

[36] E. van Sebille, S. Waterman, A. Barthel, R. Lumpkin, S.R. Keating, C. Fogwill, & C. Turney (2015). *Pairwise surface drifter separation in the western Pacific sector of the Southern Ocean.* Journal of Geophysical Research: Oceans, Vol. 120, pp. 6769-6781.

[37] M. Cancet, D. Griffin, M. Cahill, B. Chapron, J. Johannessen, & C. Donlon (2019). *Evaluation of GlobCurrent Surface Ocean Current Products: A Case Study in Australia.* Remote Sensing of Environment, Vol. 220, pp. 71-93.

[38] H. Feng, D. Vandemark, J. Levin, & J. Wilkin (2018). *Examining the Accuracy of GlobCurrent Upper Ocean Velocity Data Products on the Northwestern Atlantic Shelf.* Remote Sensing, Vol. 10, No. 8, p. 1205.

[39] S.S. Sadri & R.C. Thompson (2014). *On the quantity and composition of floating plastic debris entering and leaving the Tamar Estuary, Southwest England.* Marine Pollution Bulletin, Vol. 81, pp. 55-60.

A Code

The Python code used for the modelling of particle advection by tidal currents is shown below.

```
"""
A model for particle advection by M2, S2, K1 and O1 tidal currents
"""

from parcels import Field, FieldSet
import datetime
import math


t0 = datetime.datetime(1900,1,1,0,0) # origin of time
starttime = datetime.datetime(2002,1,1,0,0) # time when the simulation starts


""" ----- Creating the FieldSet with GlobCurrent data ----- """

# We use the daily mean geostrophic + Ekman current
# from January 1st, 2002 until December 31st, 2014
filenames = {'U': '/scratch/Miriam/GlobCurrentData/20*.nc',
             'V': '/scratch/Miriam/GlobCurrentData/20*.nc',
             'borU': '/scratch/Miriam/GlobCurrentData/boundary_velocitiesTotal.nc',
             'borV': '/scratch/Miriam/GlobCurrentData/boundary_velocitiesTotal.nc'}
variables = {'U': 'eastward_eulerian_current_velocity',
             'V': 'northward_eulerian_current_velocity',
             'borU': 'MaskUvel', # anti-beaching boundary current
             'borV': 'MaskVvel'}
dimensions = {'lat': 'lat',
              'lon': 'lon',
              'time': 'time'}
fieldset = FieldSet.from_netcdf(filenames, variables, dimensions, allow_time_extrapolation=True)
fieldset.add_constant('t0rel', (starttime - t0).total_seconds())


""" ----- Creating the tidal Fields using FES2014 dataset ----- """

files_eastward = '/scratch/Miriam/FESData/eastward_velocity/'
files_northward = '/scratch/Miriam/FESData/northward_velocity/'

dimensions_Ua = {'data': 'Ua', 'lat': 'lat', 'lon': 'lon'}
dimensions_Ug = {'data': 'Ug', 'lat': 'lat', 'lon': 'lon'}
dimensions_Va = {'data': 'Va', 'lat': 'lat', 'lon': 'lon'}
dimensions_Vg = {'data': 'Vg', 'lat': 'lat', 'lon': 'lon'}

deg2rad = math.pi/180.0

""" --- M2 component --- """

filename_UM2 = files_eastward + 'm2.nc'
filename_VM2 = files_northward + 'm2.nc'

UaM2 = Field.from_netcdf(filename_UM2, 'UaM2', dimensions_Ua, fieldtype='U')
UaM2.set_scaling_factor(1e-2) # convert from cm/s to m/s
UgM2 = Field.from_netcdf(filename_UM2, 'UgM2', dimensions_Ug)
UgM2.set_scaling_factor(deg2rad) # convert from degrees to radians
VaM2 = Field.from_netcdf(filename_VM2, 'VaM2', dimensions_Va, fieldtype='V')
VaM2.set_scaling_factor(1e-2)
VgM2 = Field.from_netcdf(filename_VM2, 'VgM2', dimensions_Vg)
VgM2.set_scaling_factor(deg2rad)
```

```
fieldset.add_field(UaM2) # eastward amplitude
fieldset.add_field(UgM2) # eastward phase shift
fieldset.add_field(VaM2) # northward amplitude
fieldset.add_field(VgM2) # northward phase shift

omega_M2 = 28.9841042 # angular frequency of M2 in degrees per hour
fieldset.add_constant('omegaM2', (omega_M2 * deg2rad) / 3600.0) # in radians per second

""" --- S2 component --- """

filename_US2 = files_eastward + 's2.nc'
filename_VS2 = files_northward + 's2.nc'

UaS2 = Field.from_netcdf(filename_US2, 'UaS2', dimensions_Ua, fieldtype='U')
UaS2.set_scaling_factor(1e-2)
UgS2 = Field.from_netcdf(filename_US2, 'UgS2', dimensions_Ug)
UgS2.set_scaling_factor(deg2rad)
VaS2 = Field.from_netcdf(filename_VS2, 'VaS2', dimensions_Va, fieldtype='V')
VaS2.set_scaling_factor(1e-2)
VgS2 = Field.from_netcdf(filename_VS2, 'VgS2', dimensions_Vg)
VgS2.set_scaling_factor(deg2rad)

fieldset.add_field(UaS2)
fieldset.add_field(UgS2)
fieldset.add_field(VaS2)
fieldset.add_field(VgS2)

omega_S2 = 30.0000000
fieldset.add_constant('omegaS2', (omega_S2 * deg2rad) / 3600.0)

""" --- K1 component --- """

filename_UK1 = files_eastward + 'k1.nc'
filename_VK1 = files_northward + 'k1.nc'

UaK1 = Field.from_netcdf(filename_UK1, 'UaK1', dimensions_Ua, fieldtype='U')
UaK1.set_scaling_factor(1e-2)
UgK1 = Field.from_netcdf(filename_UK1, 'UgK1', dimensions_Ug)
UgK1.set_scaling_factor(deg2rad)
VaK1 = Field.from_netcdf(filename_VK1, 'VaK1', dimensions_Va, fieldtype='V')
VaK1.set_scaling_factor(1e-2)
VgK1 = Field.from_netcdf(filename_VK1, 'VgK1', dimensions_Vg)
VgK1.set_scaling_factor(deg2rad)

fieldset.add_field(UaK1)
fieldset.add_field(UgK1)
fieldset.add_field(VaK1)
fieldset.add_field(VgK1)

omega_K1 = 15.0410686
fieldset.add_constant('omegaK1', (omega_K1 * deg2rad) / 3600.0)

""" --- O1 component --- """

filename_UO1 = files_eastward + 'o1.nc'
filename_VO1 = files_northward + 'o1.nc'

UaO1 = Field.from_netcdf(filename_UO1, 'UaO1', dimensions_Ua, fieldtype='U')
UaO1.set_scaling_factor(1e-2)
UgO1 = Field.from_netcdf(filename_UO1, 'UgO1', dimensions_Ug)
UgO1.set_scaling_factor(deg2rad)
VaO1 = Field.from_netcdf(filename_VO1, 'VaO1', dimensions_Va, fieldtype='V')
```

```
Va01.set_scaling_factor(1e-2)
Vg01 = Field.from_netcdf(filename_V01, 'Vg01', dimensions_Vg)
Vg01.set_scaling_factor(deg2rad)

fieldset.add_field(Ua01)
fieldset.add_field(Ug01)
fieldset.add_field(Va01)
fieldset.add_field(Vg01)

omega_01 = 13.9430356
fieldset.add_constant('omega01', (omega_01 * deg2rad) / 3600.0)


# Add a zonal periodic halo to all the fields in fieldset
fieldset.add_periodic_halo(zonal=True)




def TidalMotionM2S2K1O1(particle, fieldset, time, dt):
    """
    Kernel that calculates tidal currents U and V due to M2, S2, K1 and O1 tide
    at particle location and time, and advects the particle in these currents using RK4
    Calculations based on Doodson (1921) and Schureman (1958)
    """
    fs = fieldset

    # Number of Julian centuries that have passed between t0 and time
    t = ((time + fieldset.t0rel)/86400.0)/36525.0

    # Define constants to compute astronomical variables T, h, s, N (all in degrees)
    # (source: FES2014 code)
    cT0 = 180.0
    ch0 = 280.1895
    cs0 = 277.0248
    cN0 = 259.1568; cN1 = -1934.1420
    deg2rad = math.pi/180.0

    # Calculation of factors T, h, s at t0 (source: Doodson (1921))
    T0 = math.fmod(cT0, 360.0) * deg2rad
    h0 = math.fmod(ch0, 360.0) * deg2rad
    s0 = math.fmod(cs0, 360.0) * deg2rad

    # Calculation of V(t0) (source: Schureman (1958))
    V_M2 = 2*T0 + 2*h0 - 2*s0
    V_S2 = 2*T0
    V_K1 = T0 + h0 - 0.5*math.pi
    V_O1 = T0 + h0 - 2*s0 + 0.5*math.pi

    # Calculation of factors N, I, nu, xi at time (source: Schureman (1958))
    # Since these factors change only very slowly over time,
    # we take them as constant over the time step dt
    N = math.fmod(cN0 + cN1*t, 360.0) * deg2rad
    I = math.acos(0.91370 - 0.03569*math.cos(N))
    tanN = math.tan(0.5*N)
    at1 = math.atan(1.01883 * tanN)
    at2 = math.atan(0.64412 * tanN)
    nu = at1 - at2
    xi = -at1 - at2 + N
    nuprim = math.atan(math.sin(2*I) * math.sin(nu)/(math.sin(2*I)*math.cos(nu) + 0.3347))

    # Calculation of u, f at current time (source: Schureman (1958))
```

```
u_M2 = 2*xi - 2*nu
f_M2 = (math.cos(0.5*I))**4/0.9154
u_S2 = 0
f_S2 = 1
u_K1 = -nuprim
f_K1 = math.sqrt(0.8965*(math.sin(2*I))**2 + 0.6001*math.sin(2*I)*math.cos(nu) + 0.1006)
u_O1 = 2*xi - nu
f_O1 = math.sin(I)*(math.cos(0.5*I))**2/0.3800

# Fourth-order Runge-Kutta methode to advect particle in tidal currents

# ----------------------- STEP 1 -----------------------
# Tidal fields have longitudes defined from 0...360 degrees (so -180...0 --> 180...360)
if particle.lon < 0:
    lon = particle.lon + 360
else:
    lon = particle.lon

# Zonal amplitudes and phaseshifts at particle location and time
Uampl_M2_1 = f_M2 * fs.UaM2[time, lon, particle.lat, particle.depth]
Upha_M2_1 = V_M2 + u_M2 - fs.UgM2[time, lon, particle.lat, particle.depth]
Uampl_S2_1 = f_S2 * fs.UaS2[time, lon, particle.lat, particle.depth]
Upha_S2_1 = V_S2 + u_S2 - fs.UgS2[time, lon, particle.lat, particle.depth]
Uampl_K1_1 = f_K1 * fs.UaK1[time, lon, particle.lat, particle.depth]
Upha_K1_1 = V_K1 + u_K1 - fs.UgK1[time, lon, particle.lat, particle.depth]
Uampl_O1_1 = f_O1 * fs.UaO1[time, lon, particle.lat, particle.depth]
Upha_O1_1 = V_O1 + u_O1 - fs.UgO1[time, lon, particle.lat, particle.depth]
# Meridional amplitudes and phaseshifts at particle location and time
Vampl_M2_1 = f_M2 * fs.VaM2[time, lon, particle.lat, particle.depth]
Vpha_M2_1 = V_M2 + u_M2 - fs.VgM2[time, lon, particle.lat, particle.depth]
Vampl_S2_1 = f_S2 * fs.VaS2[time, lon, particle.lat, particle.depth]
Vpha_S2_1 = V_S2 + u_S2 - fs.VgS2[time, lon, particle.lat, particle.depth]
Vampl_K1_1 = f_K1 * fs.VaK1[time, lon, particle.lat, particle.depth]
Vpha_K1_1 = V_K1 + u_K1 - fs.VgK1[time, lon, particle.lat, particle.depth]
Vampl_O1_1 = f_O1 * fs.VaO1[time, lon, particle.lat, particle.depth]
Vpha_O1_1 = V_O1 + u_O1 - fs.VgO1[time, lon, particle.lat, particle.depth]
# Zonal and meridional tidal currents;
# time + fieldset.t0rel = number of seconds elapsed between t0 and time
Uvel_M2_1 = Uampl_M2_1 * math.cos(fs.omegaM2 * (time + fs.t0rel) + Upha_M2_1)
Uvel_S2_1 = Uampl_S2_1 * math.cos(fs.omegaS2 * (time + fs.t0rel) + Upha_S2_1)
Uvel_K1_1 = Uampl_K1_1 * math.cos(fs.omegaK1 * (time + fs.t0rel) + Upha_K1_1)
Uvel_O1_1 = Uampl_O1_1 * math.cos(fs.omegaO1 * (time + fs.t0rel) + Upha_O1_1)
Vvel_M2_1 = Vampl_M2_1 * math.cos(fs.omegaM2 * (time + fs.t0rel) + Vpha_M2_1)
Vvel_S2_1 = Vampl_S2_1 * math.cos(fs.omegaS2 * (time + fs.t0rel) + Vpha_S2_1)
Vvel_K1_1 = Vampl_K1_1 * math.cos(fs.omegaK1 * (time + fs.t0rel) + Vpha_K1_1)
Vvel_O1_1 = Vampl_O1_1 * math.cos(fs.omegaO1 * (time + fs.t0rel) + Vpha_O1_1)
# Total zonal and meridional velocity
U1 = Uvel_M2_1 + Uvel_S2_1 + Uvel_K1_1 + Uvel_O1_1 # total zonal velocity
V1 = Vvel_M2_1 + Vvel_S2_1 + Vvel_K1_1 + Vvel_O1_1 # total meridional velocity
# New lon + lat
lon1, lat1 = (particle.lon + U1*0.5*dt, particle.lat + V1*0.5*dt)

# ----------------------- STEP 2 -----------------------
if lon1 < 0:
    lon1 += 360

# Zonal amplitudes and phaseshifts at particle location and time
Uampl_M2_2 = f_M2 * fs.UaM2[time + 0.5*dt, lon1, lat1, particle.depth]
Upha_M2_2 = V_M2 + u_M2 - fs.UgM2[time + 0.5*dt, lon1, lat1, particle.depth]
Uampl_S2_2 = f_S2 * fs.UaS2[time + 0.5*dt, lon1, lat1, particle.depth]
Upha_S2_2 = V_S2 + u_S2 - fs.UgS2[time + 0.5*dt, lon1, lat1, particle.depth]
Uampl_K1_2 = f_K1 * fs.UaK1[time + 0.5*dt, lon1, lat1, particle.depth]
```

```
    Upha_K1_2 = V_K1 + u_K1 - fs.UgK1[time + 0.5*dt, lon1, lat1, particle.depth]
    Uampl_O1_2 = f_O1 * fs.UaO1[time + 0.5*dt, lon1, lat1, particle.depth]
    Upha_O1_2 = V_O1 + u_O1 - fs.UgO1[time + 0.5*dt, lon1, lat1, particle.depth]
    # Meridional amplitudes and phaseshifts at particle location and time
    Vampl_M2_2 = f_M2 * fs.VaM2[time + 0.5*dt, lon1, lat1, particle.depth]
    Vpha_M2_2 = V_M2 + u_M2 - fs.VgM2[time + 0.5*dt, lon1, lat1, particle.depth]
    Vampl_S2_2 = f_S2 * fs.VaS2[time + 0.5*dt, lon1, lat1, particle.depth]
    Vpha_S2_2 = V_S2 + u_S2 - fs.VgS2[time + 0.5*dt, lon1, lat1, particle.depth]
    Vampl_K1_2 = f_K1 * fs.VaK1[time + 0.5*dt, lon1, lat1, particle.depth]
    Vpha_K1_2 = V_K1 + u_K1 - fs.VgK1[time + 0.5*dt, lon1, lat1, particle.depth]
    Vampl_O1_2 = f_O1 * fs.VaO1[time + 0.5*dt, lon1, lat1, particle.depth]
    Vpha_O1_2 = V_O1 + u_O1 - fs.VgO1[time + 0.5*dt, lon1, lat1, particle.depth]
    # Zonal and meridional tidal currents
    Uvel_M2_2 = Uampl_M2_2 * math.cos(fs.omegaM2 * (time + 0.5*dt + fs.t0rel) + Upha_M2_2)
    Uvel_S2_2 = Uampl_S2_2 * math.cos(fs.omegaS2 * (time + 0.5*dt + fs.t0rel) + Upha_S2_2)
    Uvel_K1_2 = Uampl_K1_2 * math.cos(fs.omegaK1 * (time + 0.5*dt + fs.t0rel) + Upha_K1_2)
    Uvel_O1_2 = Uampl_O1_2 * math.cos(fs.omegaO1 * (time + 0.5*dt + fs.t0rel) + Upha_O1_2)
    Vvel_M2_2 = Vampl_M2_2 * math.cos(fs.omegaM2 * (time + 0.5*dt + fs.t0rel) + Vpha_M2_2)
    Vvel_S2_2 = Vampl_S2_2 * math.cos(fs.omegaS2 * (time + 0.5*dt + fs.t0rel) + Vpha_S2_2)
    Vvel_K1_2 = Vampl_K1_2 * math.cos(fs.omegaK1 * (time + 0.5*dt + fs.t0rel) + Vpha_K1_2)
    Vvel_O1_2 = Vampl_O1_2 * math.cos(fs.omegaO1 * (time + 0.5*dt + fs.t0rel) + Vpha_O1_2)
    # Total zonal and meridional velocity
    U2 = Uvel_M2_2 + Uvel_S2_2 + Uvel_K1_2 + Uvel_O1_2 # total zonal velocity
    V2 = Vvel_M2_2 + Vvel_S2_2 + Vvel_K1_2 + Vvel_O1_2 # total meridional velocity
    # New lon + lat
    lon2, lat2 = (particle.lon + U2*0.5*dt, particle.lat + V2*0.5*dt)

    # ----------------------- STEP 3 ----------------------
    if lon2 < 0:
        lon2 += 360

    # Zonal amplitudes and phaseshifts at particle location and time
    Uampl_M2_3 = f_M2 * fs.UaM2[time + 0.5*dt, lon2, lat2, particle.depth]
    Upha_M2_3 = V_M2 + u_M2 - fs.UgM2[time + 0.5*dt, lon2, lat2, particle.depth]
    Uampl_S2_3 = f_S2 * fs.UaS2[time + 0.5*dt, lon2, lat2, particle.depth]
    Upha_S2_3 = V_S2 + u_S2 - fs.UgS2[time + 0.5*dt, lon2, lat2, particle.depth]
    Uampl_K1_3 = f_K1 * fs.UaK1[time + 0.5*dt, lon2, lat2, particle.depth]
    Upha_K1_3 = V_K1 + u_K1 - fs.UgK1[time + 0.5*dt, lon2, lat2, particle.depth]
    Uampl_O1_3 = f_O1 * fs.UaO1[time + 0.5*dt, lon2, lat2, particle.depth]
    Upha_O1_3 = V_O1 + u_O1 - fs.UgO1[time + 0.5*dt, lon2, lat2, particle.depth]
    # Meridional amplitudes and phaseshifts at particle location and time
    Vampl_M2_3 = f_M2 * fs.VaM2[time + 0.5*dt, lon2, lat2, particle.depth]
    Vpha_M2_3 = V_M2 + u_M2 - fs.VgM2[time + 0.5*dt, lon2, lat2, particle.depth]
    Vampl_S2_3 = f_S2 * fs.VaS2[time + 0.5*dt, lon2, lat2, particle.depth]
    Vpha_S2_3 = V_S2 + u_S2 - fs.VgS2[time + 0.5*dt, lon2, lat2, particle.depth]
    Vampl_K1_3 = f_K1 * fs.VaK1[time + 0.5*dt, lon2, lat2, particle.depth]
    Vpha_K1_3 = V_K1 + u_K1 - fs.VgK1[time + 0.5*dt, lon2, lat2, particle.depth]
    Vampl_O1_3 = f_O1 * fs.VaO1[time + 0.5*dt, lon2, lat2, particle.depth]
    Vpha_O1_3 = V_O1 + u_O1 - fs.VgO1[time + 0.5*dt, lon2, lat2, particle.depth]
    # Zonal and meridional tidal currents
    Uvel_M2_3 = Uampl_M2_3 * math.cos(fs.omegaM2 * (time + 0.5*dt + fs.t0rel) + Upha_M2_3)
    Uvel_S2_3 = Uampl_S2_3 * math.cos(fs.omegaS2 * (time + 0.5*dt + fs.t0rel) + Upha_S2_3)
    Uvel_K1_3 = Uampl_K1_3 * math.cos(fs.omegaK1 * (time + 0.5*dt + fs.t0rel) + Upha_K1_3)
    Uvel_O1_3 = Uampl_O1_3 * math.cos(fs.omegaO1 * (time + 0.5*dt + fs.t0rel) + Upha_O1_3)
    Vvel_M2_3 = Vampl_M2_3 * math.cos(fs.omegaM2 * (time + 0.5*dt + fs.t0rel) + Vpha_M2_3)
    Vvel_S2_3 = Vampl_S2_3 * math.cos(fs.omegaS2 * (time + 0.5*dt + fs.t0rel) + Vpha_S2_3)
    Vvel_K1_3 = Vampl_K1_3 * math.cos(fs.omegaK1 * (time + 0.5*dt + fs.t0rel) + Vpha_K1_3)
    Vvel_O1_3 = Vampl_O1_3 * math.cos(fs.omegaO1 * (time + 0.5*dt + fs.t0rel) + Vpha_O1_3)
    # Total zonal and meridional velocity
    U3 = Uvel_M2_3 + Uvel_S2_3 + Uvel_K1_3 + Uvel_O1_3 # total zonal velocity
    V3 = Vvel_M2_3 + Vvel_S2_3 + Vvel_K1_3 + Vvel_O1_3 # total meridional velocity
    # New lon + lat
```

```
    lon3, lat3 = (particle.lon + U3*dt, particle.lat + V3*dt)

    # ----------------------- STEP 4 ----------------------
    if lon3 < 0:
        lon3 += 360

    # Zonal amplitudes and phaseshifts at particle location and time
    Uampl_M2_4 = f_M2 * fs.UaM2[time + dt, lon3, lat3, particle.depth]
    Upha_M2_4 = V_M2 + u_M2 - fs.UgM2[time + dt, lon3, lat3, particle.depth]
    Uampl_S2_4 = f_S2 * fs.UaS2[time + dt, lon3, lat3, particle.depth]
    Upha_S2_4 = V_S2 + u_S2 - fs.UgS2[time + dt, lon3, lat3, particle.depth]
    Uampl_K1_4 = f_K1 * fs.UaK1[time + dt, lon3, lat3, particle.depth]
    Upha_K1_4 = V_K1 + u_K1 - fs.UgK1[time + dt, lon3, lat3, particle.depth]
    Uampl_O1_4 = f_O1 * fs.UaO1[time + dt, lon3, lat3, particle.depth]
    Upha_O1_4 = V_O1 + u_O1 - fs.UgO1[time + dt, lon3, lat3, particle.depth]
    # Meridional amplitudes and phaseshifts at particle location and time
    Vampl_M2_4 = f_M2 * fs.VaM2[time + dt, lon3, lat3, particle.depth]
    Vpha_M2_4 = V_M2 + u_M2 - fs.VgM2[time + dt, lon3, lat3, particle.depth]
    Vampl_S2_4 = f_S2 * fs.VaS2[time + dt, lon3, lat3, particle.depth]
    Vpha_S2_4 = V_S2 + u_S2 - fs.VgS2[time + dt, lon3, lat3, particle.depth]
    Vampl_K1_4 = f_K1 * fs.VaK1[time + dt, lon3, lat3, particle.depth]
    Vpha_K1_4 = V_K1 + u_K1 - fs.VgK1[time + dt, lon3, lat3, particle.depth]
    Vampl_O1_4 = f_O1 * fs.VaO1[time + dt, lon3, lat3, particle.depth]
    Vpha_O1_4 = V_O1 + u_O1 - fs.VgO1[time + dt, lon3, lat3, particle.depth]
    # Zonal and meridional tidal currents
    Uvel_M2_4 = Uampl_M2_4 * math.cos(fs.omegaM2 * (time + dt + fs.t0rel) + Upha_M2_4)
    Uvel_S2_4 = Uampl_S2_4 * math.cos(fs.omegaS2 * (time + dt + fs.t0rel) + Upha_S2_4)
    Uvel_K1_4 = Uampl_K1_4 * math.cos(fs.omegaK1 * (time + dt + fs.t0rel) + Upha_K1_4)
    Uvel_O1_4 = Uampl_O1_4 * math.cos(fs.omegaO1 * (time + dt + fs.t0rel) + Upha_O1_4)
    Vvel_M2_4 = Vampl_M2_4 * math.cos(fs.omegaM2 * (time + dt + fs.t0rel) + Vpha_M2_4)
    Vvel_S2_4 = Vampl_S2_4 * math.cos(fs.omegaS2 * (time + dt + fs.t0rel) + Vpha_S2_4)
    Vvel_K1_4 = Vampl_K1_4 * math.cos(fs.omegaK1 * (time + dt + fs.t0rel) + Vpha_K1_4)
    Vvel_O1_4 = Vampl_O1_4 * math.cos(fs.omegaO1 * (time + dt + fs.t0rel) + Vpha_O1_4)
    # Total zonal and meridional velocity
    U4 = Uvel_M2_4 + Uvel_S2_4 + Uvel_K1_4 + Uvel_O1_4 # total zonal velocity
    V4 = Vvel_M2_4 + Vvel_S2_4 + Vvel_K1_4 + Vvel_O1_4 # total meridional velocity

    # Finally, the new particle location:
    particle.lon += (U1 + 2*U2 + 2*U3 + U4)/6. * dt
    particle.lat += (V1 + 2*V2 + 2*V3 + V4)/6. * dt
```

B Additional figures

B.1 Density in final year of simulation

Figure 17 shows an enlarged version of Figures 10d and 10h from Section 4.1.

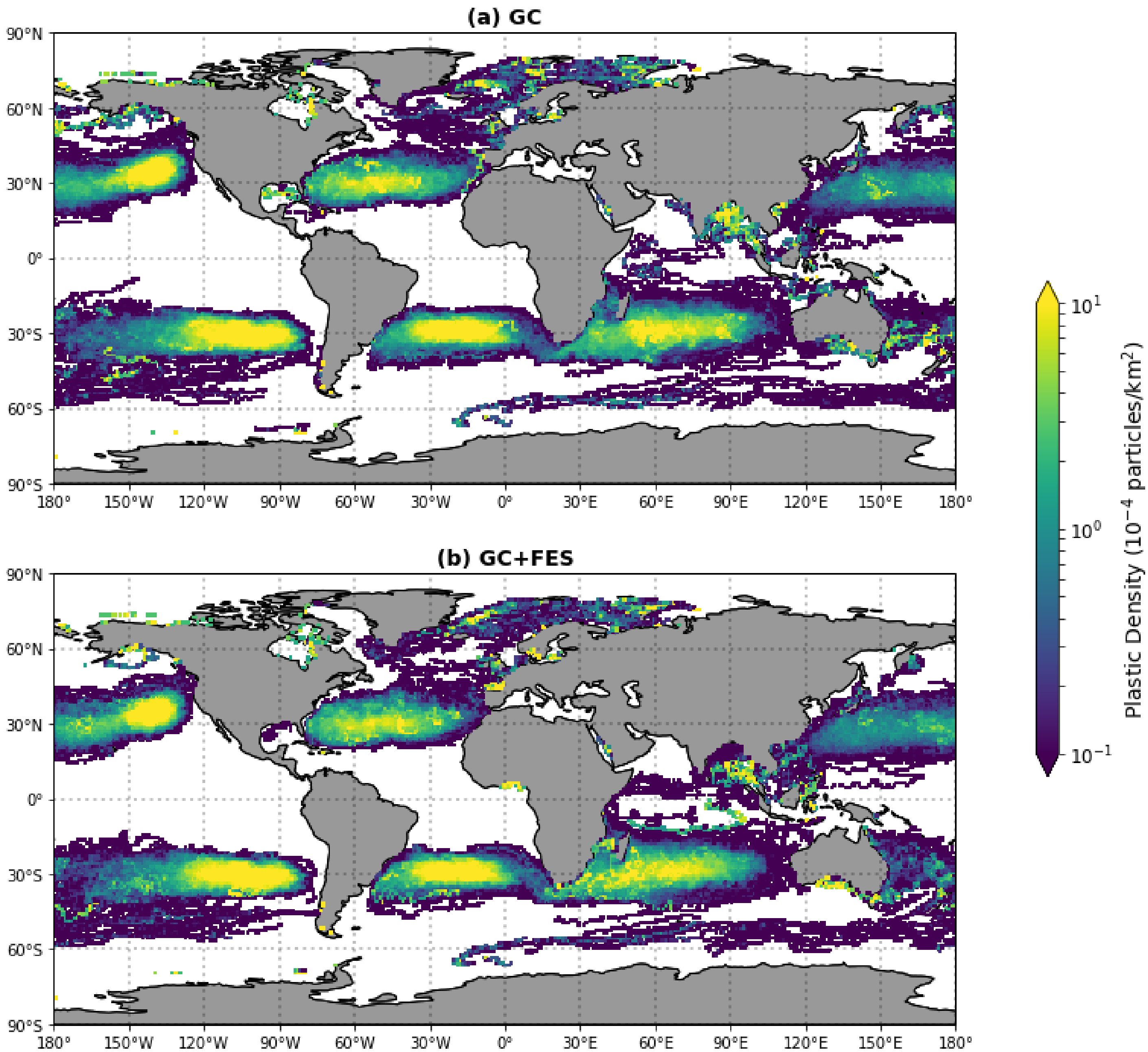

Figure 17: The average microplastic particle density for the final year of the runs without tidal currents (a) and with the main tidal currents (b).

B.2 Visualisation and comparison of TPXO and FES data

Figures 18-33 show the amplitude and phase shift data for the eastward and northward velocity component of the M_2, S_2, K_1 and O_1 tide, for the TPXO7.2 dataset and the FES2014 dataset.

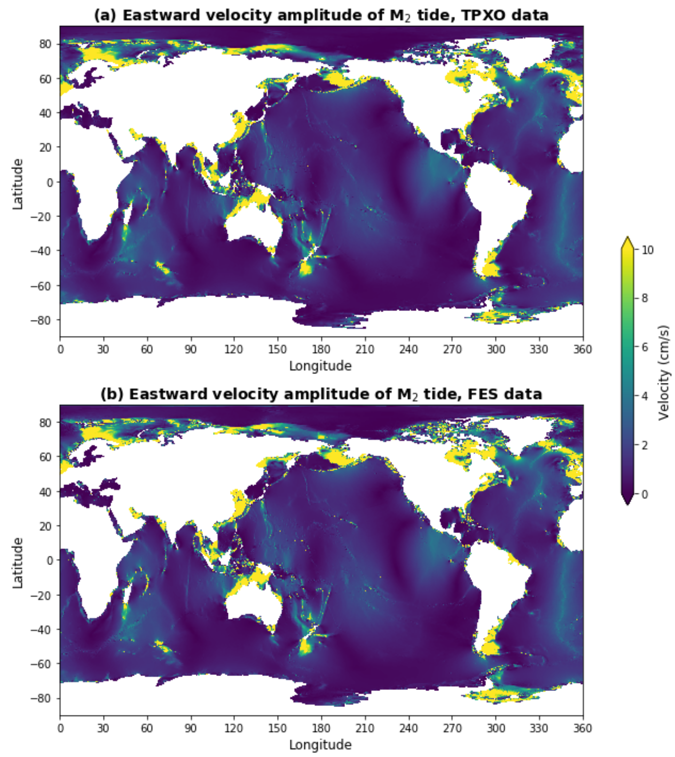

Figure 18: The eastward velocity amplitude A^U of the M_2 tide from the TPXO7.2 dataset and from the FES2014 dataset.

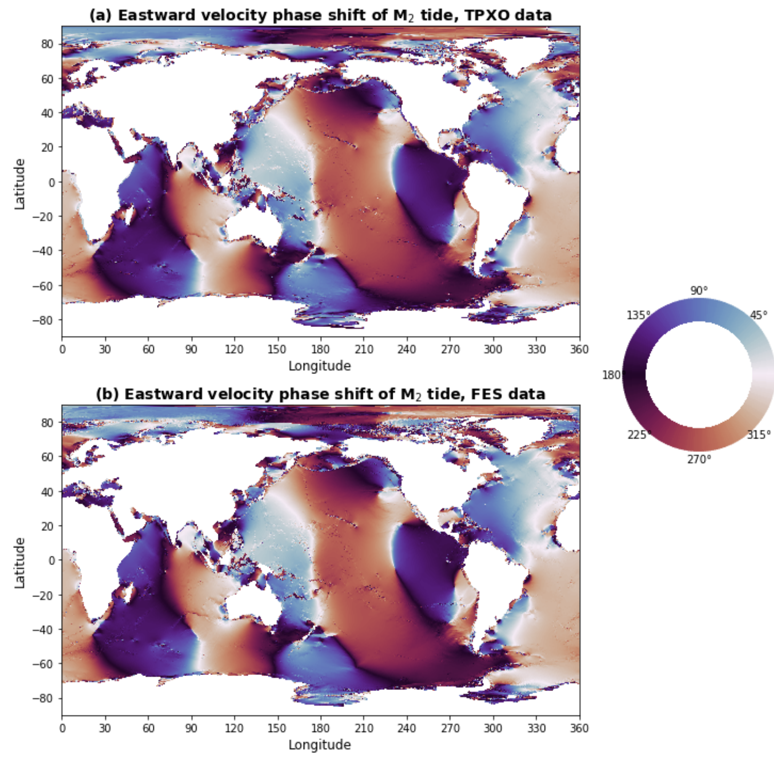

Figure 19: The eastward velocity phase shift φ^U of the M_2 tide from the TPXO7.2 dataset and from the FES2014 dataset.

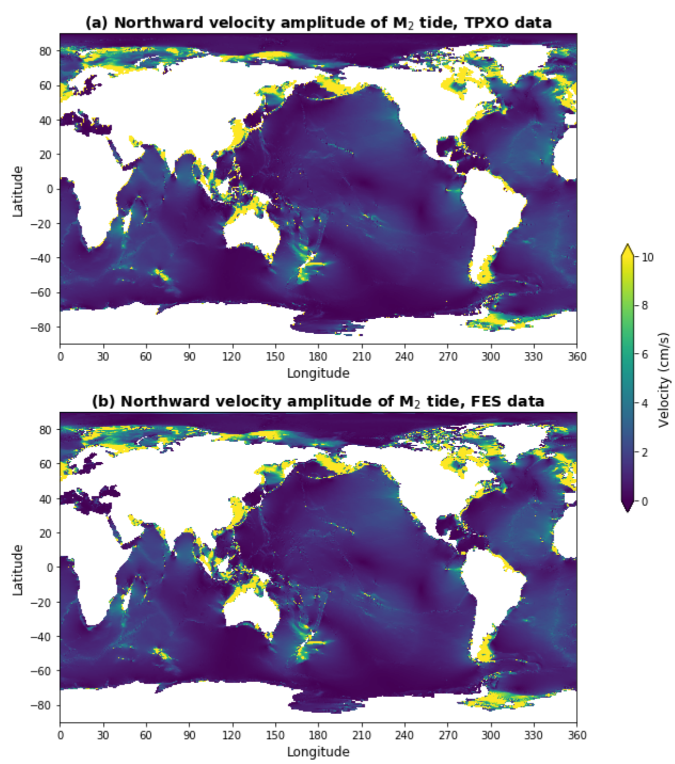

Figure 20: The northward velocity amplitude A^V of the M_2 tide from the TPXO7.2 dataset and from the FES2014 dataset.

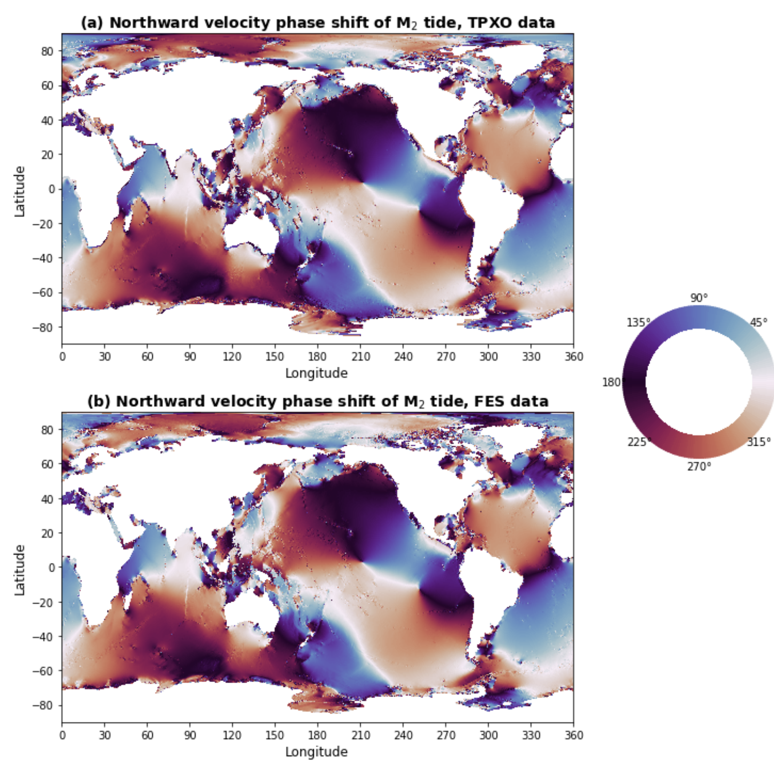

Figure 21: The northward velocity phase shift φ^V of the M_2 tide from the TPXO7.2 dataset and from the FES2014 dataset.

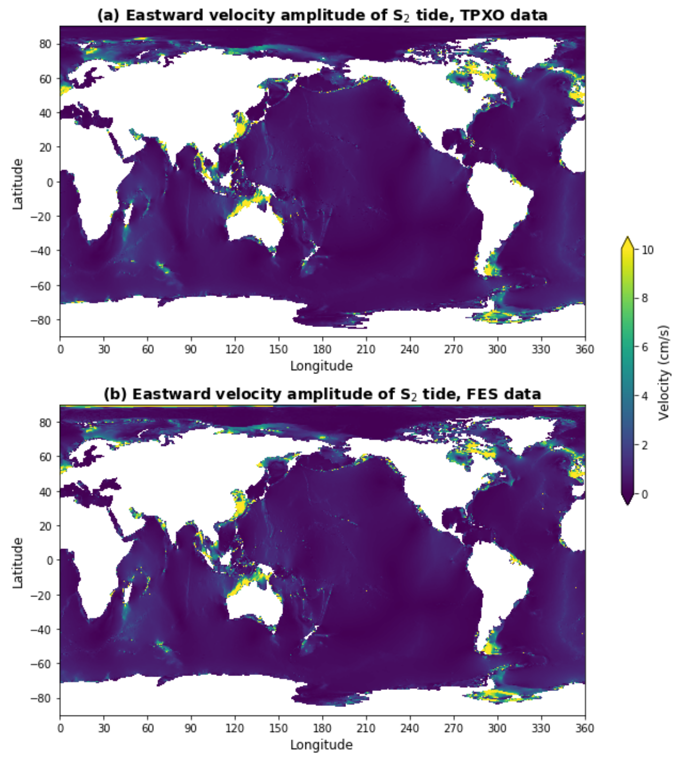

Figure 22: The eastward velocity amplitude A^U of the S_2 tide from the TPXO7.2 dataset and from the FES2014 dataset.

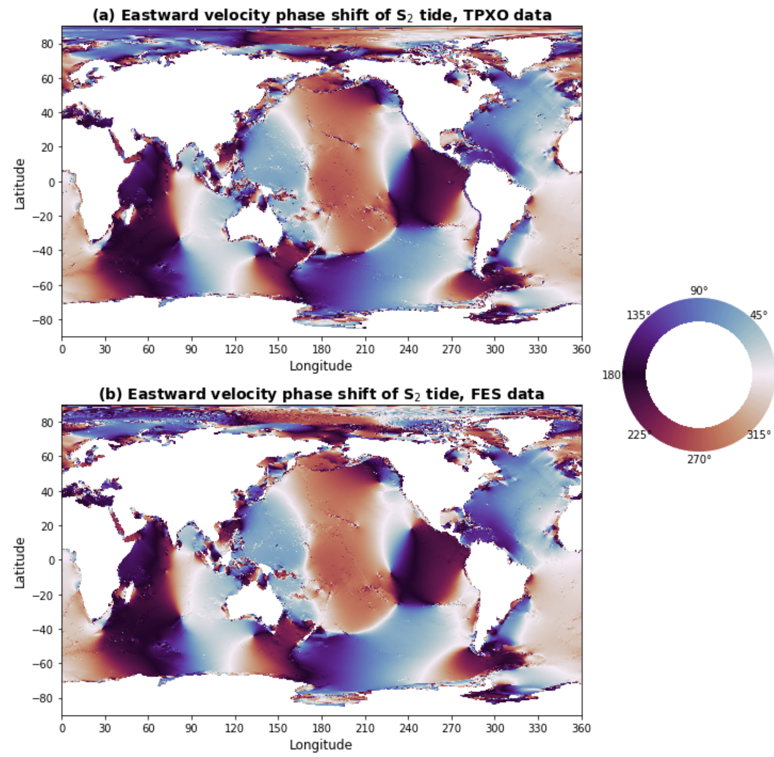

Figure 23: The eastward velocity phase shift φ^U of the S_2 tide from the TPXO7.2 dataset and from the FES2014 dataset.

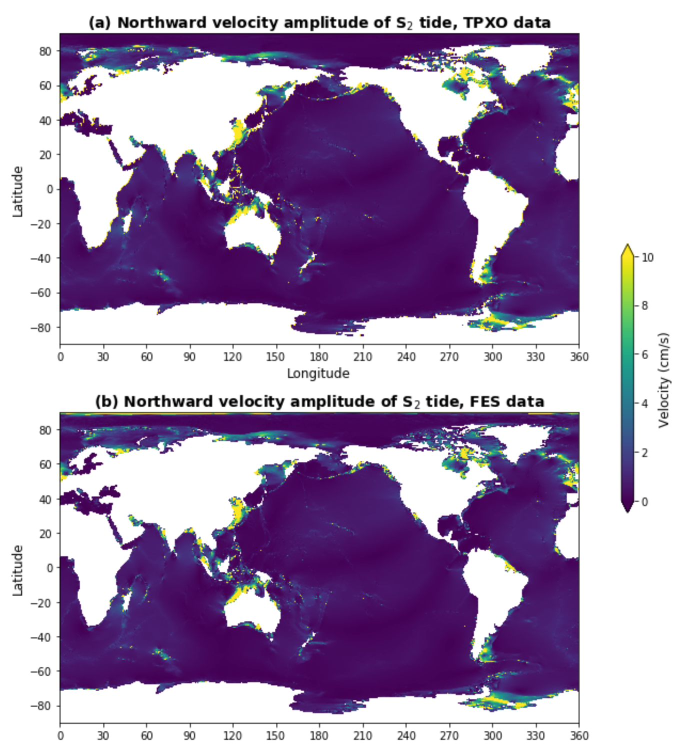

Figure 24: The northward velocity amplitude A^V of the S_2 tide from the TPXO7.2 dataset and from the FES2014 dataset.

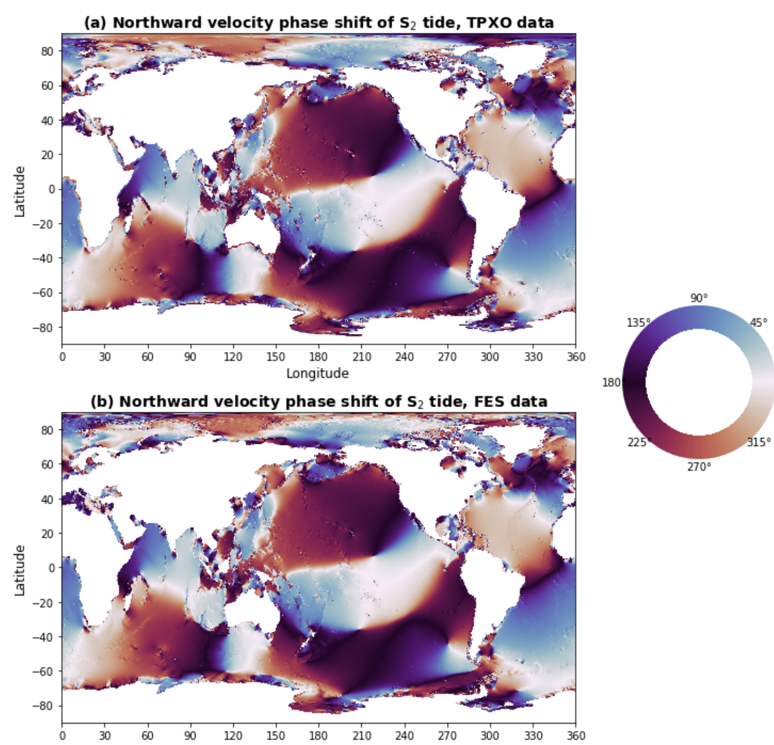

Figure 25: The northward velocity phase shift φ^V of the S_2 tide from the TPXO7.2 dataset and from the FES2014 dataset.

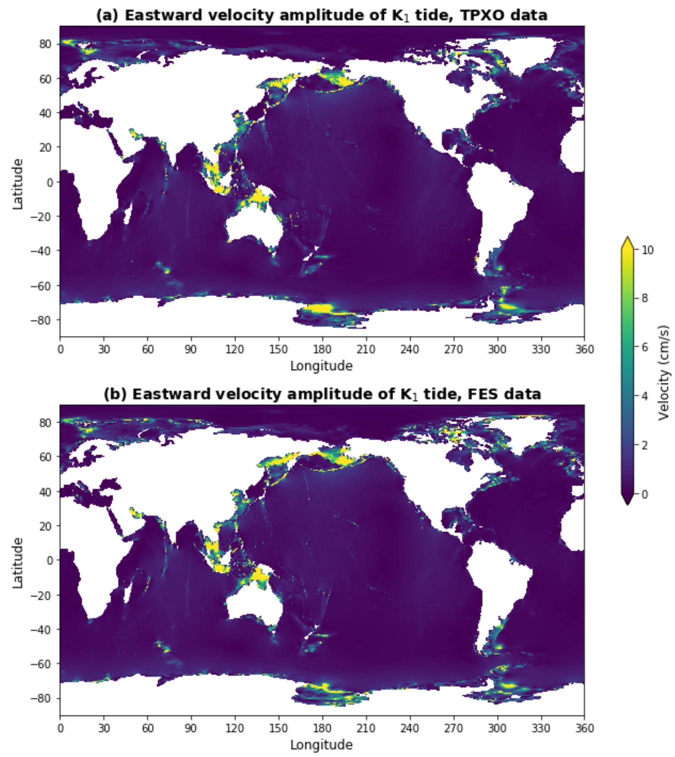

Figure 26: The eastward velocity amplitude A^U of the K_1 tide from the TPXO7.2 dataset and from the FES2014 dataset.

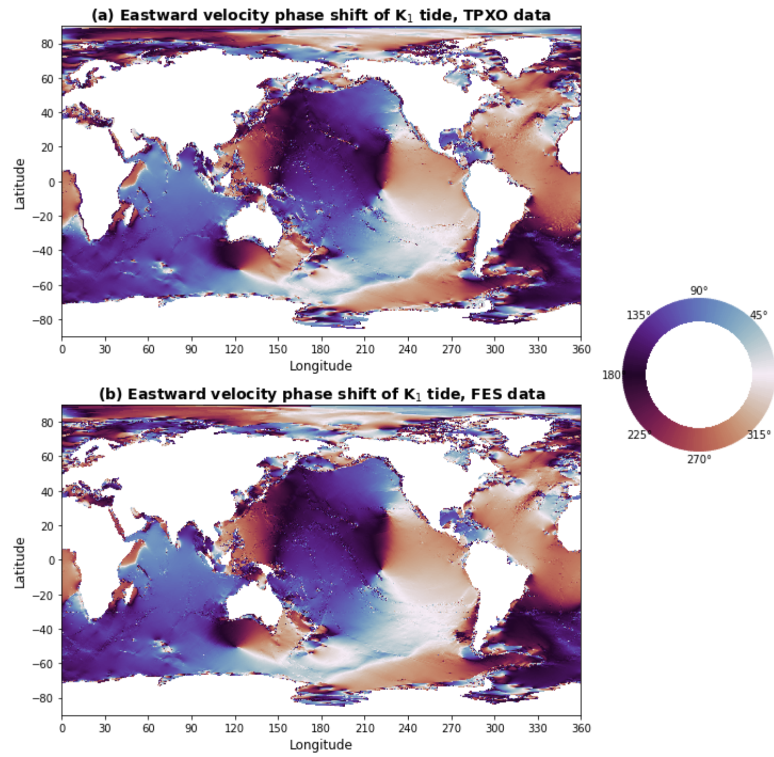

Figure 27: The eastward velocity phase shift φ^U of the K_1 tide from the TPXO7.2 dataset and from the FES2014 dataset.

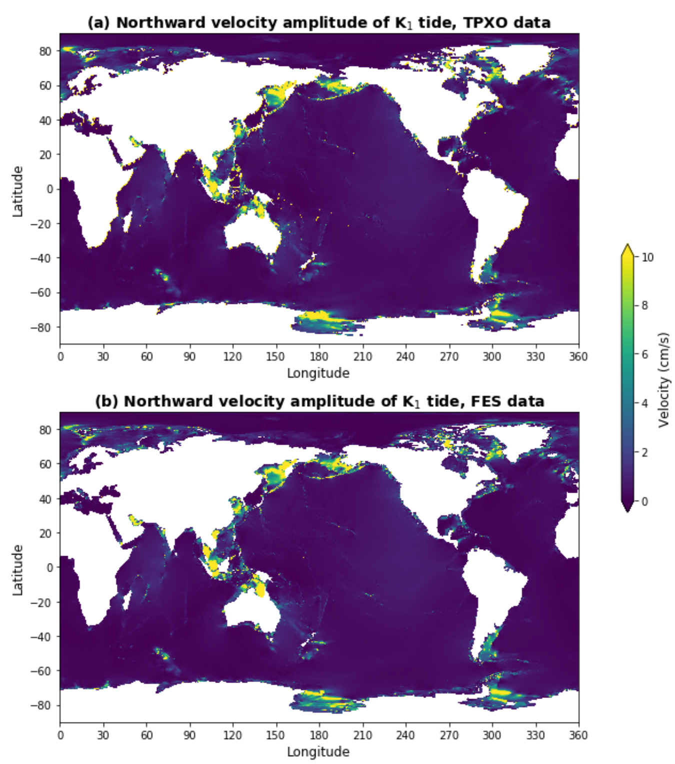

Figure 28: The northward velocity amplitude A^V of the K_1 tide from the TPXO7.2 dataset and from the FES2014 dataset.

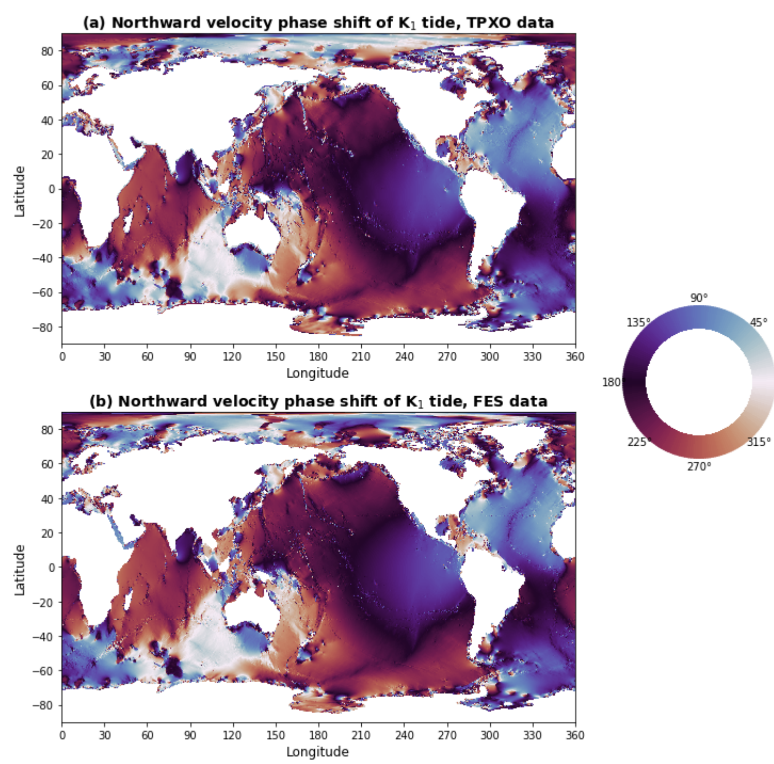

Figure 29: The northward velocity phase shift φ^V of the K_1 tide from the TPXO7.2 dataset and from the FES2014 dataset.

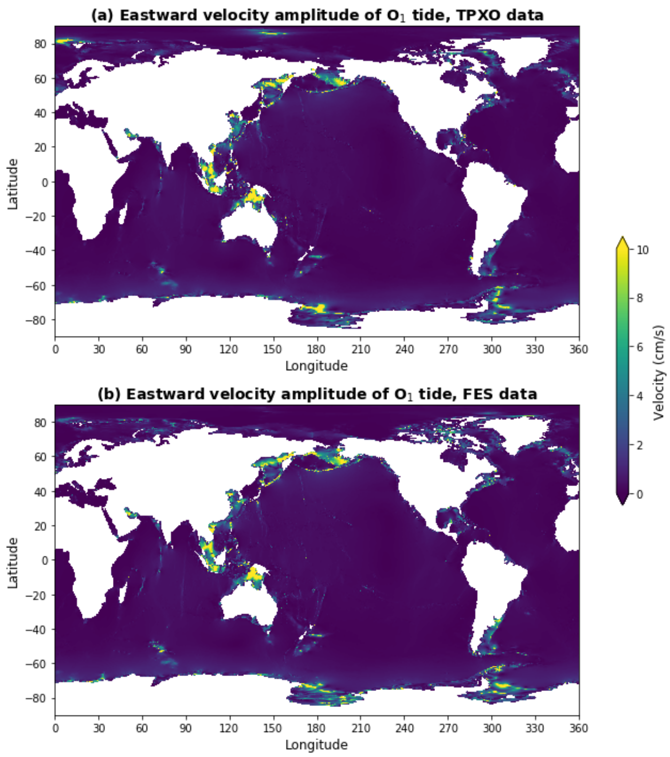

Figure 30: The eastward velocity amplitude A^U of the O_1 tide from the TPXO7.2 dataset and from the FES2014 dataset.

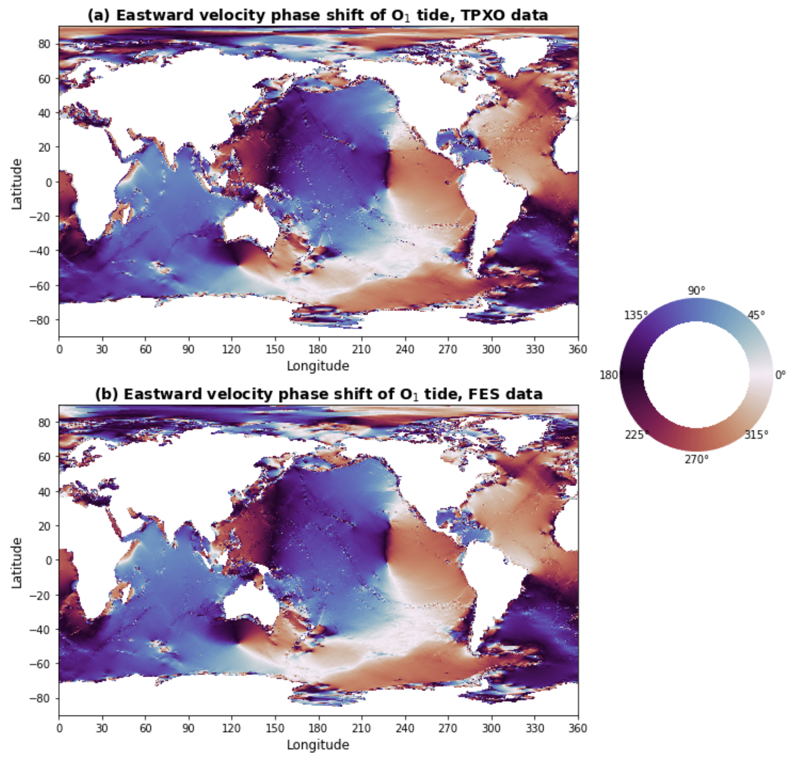

Figure 31: The eastward velocity phase shift φ^U of the O_1 tide from the TPXO7.2 dataset and from the FES2014 dataset.

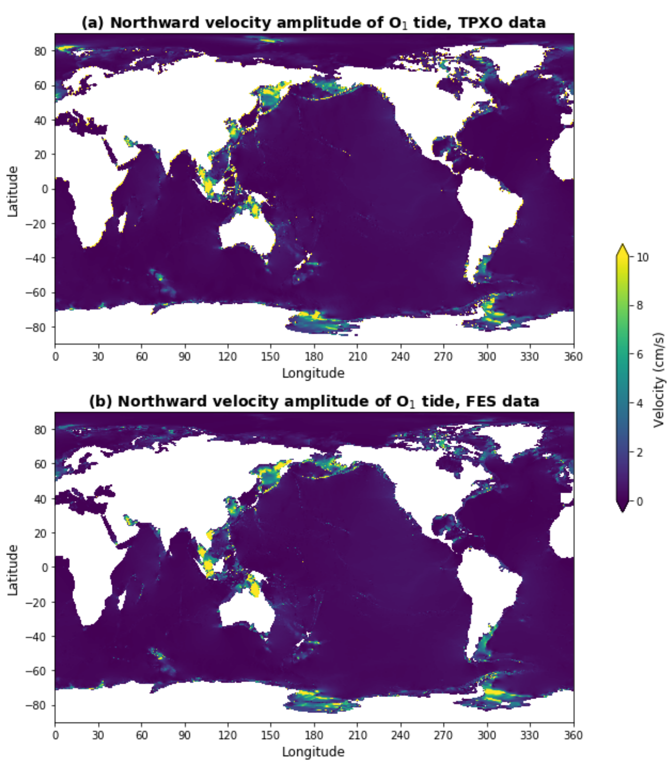

Figure 32: The northward velocity amplitude A^V of the O_1 tide from the TPXO7.2 dataset and from the FES2014 dataset.

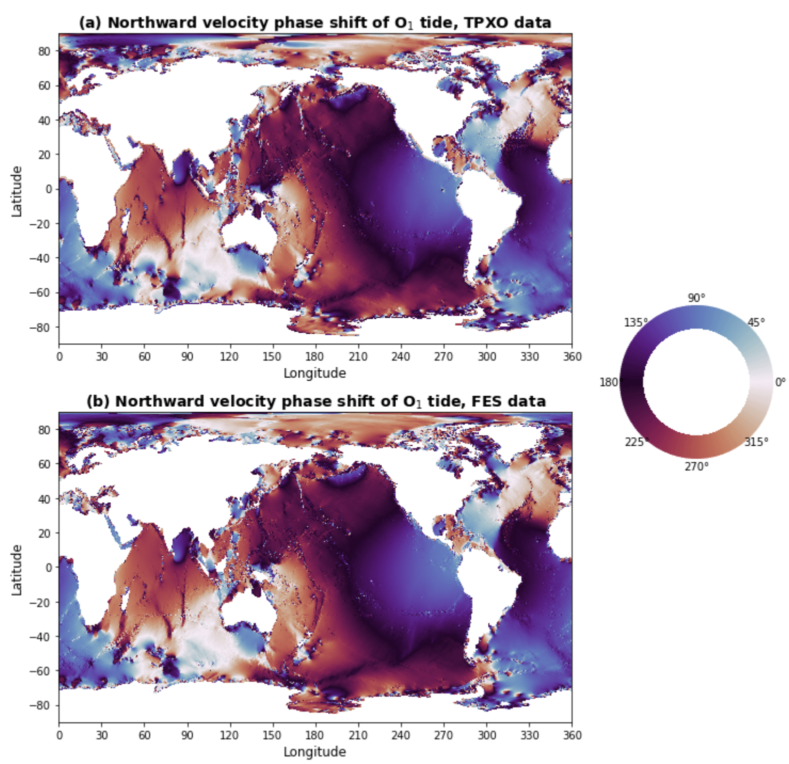

Figure 33: The northward velocity phase shift φ^V of the O_1 tide from the TPXO7.2 dataset and from the FES2014 dataset.